

Finding η Car Analogs in Nearby Galaxies Using *Spitzer*: II. Identification of An Emerging Class of Extragalactic Self-Obscured Stars

Rubab Khan¹, C. S. Kochanek^{1,2}, K. Z. Stanek^{1,2}, Jill Gerke¹

ABSTRACT

Understanding the late-stage evolution of the most massive stars such as η Carinae is challenging because no true analogs of η Car have been clearly identified in the Milky Way or other galaxies. In Khan et al. (2013), we utilized *Spitzer* IRAC images of 7 nearby ($\lesssim 4$ Mpc) galaxies to search for such analogs, and found 34 candidates with flat or red mid-IR spectral energy distributions. Here, in Paper II, we present our characterization of these candidates using multi-wavelength data from the optical through the far-IR. Our search detected no true analogs of η Car, which implies an eruption rate that is a fraction $0.01 \lesssim F \lesssim 0.19$ of the ccSN rate. This is roughly consistent with each $M_{ZAMS} \gtrsim 70M_{\odot}$ star undergoing 1 or 2 outbursts in its lifetime. However, we do identify a significant population of 18 lower luminosity ($\log(L/L_{\odot}) \simeq 5.5 - 6.0$) dusty stars. Stars enter this phase at a rate that is fraction $0.09 \lesssim F \lesssim 0.55$ of the ccSN rate, and this is consistent with all $25 < M_{ZAMS} < 60M_{\odot}$ stars undergoing an obscured phase at most lasting a few thousand years once or twice. These phases constitute a negligible fraction of post-main sequence lifetimes of massive stars, which implies that these events are likely to be associated with special periods in the evolution of the stars. The mass of the obscuring material is of order $\sim M_{\odot}$, and we simply do not find enough heavily obscured stars for these phases to represent more than a modest fraction ($\sim 10\%$ not $\sim 50\%$) of the total mass lost by these stars. In the long term, the sources that we identified will be prime candidates for detailed physical analysis with *JWST*.

Subject headings: stars: evolution, mass-loss, winds, outflows — stars: individual: Eta Carinae — galaxies: individual (M33, M81, NGC247, NGC300, NGC2403, NGC6822, NGC7793)

¹Dept. of Astronomy, The Ohio State University, 140 W. 18th Ave., Columbus, OH 43210; khan, kstanek, ckochanek@astronomy.ohio-state.edu

²Center for Cosmology and AstroParticle Physics, The Ohio State University, 191 W. Woodruff Ave., Columbus, OH 43210

1. Introduction

Despite being very rare, massive stars such as luminous blue variable (LBVs), red super giants (RSGs), and Wolf-Rayet stars (WRs) play a pivotal role in enriching the interstellar medium (ISM) through mass loss, and they are an important source of heavier elements contributing to the chemical enrichment of galaxies (e.g., Maeder 1981). The deaths of these massive stars are associated with some of the highest energy phenomena in the universe such as core-collapse supernovae (ccSNe, Smartt 2009), long-duration gamma-ray bursts (e.g., Stanek et al. 2003), neutrino bursts (e.g., Bionta et al. 1987) and gravitational wave bursts (e.g., Ott 2009). The physical mechanism, energetics and observed properties of these events depend on the structure and terminal mass of the evolved stars at core-collapse, which in turn are determined by stellar mass loss (see, e.g., review by Smith 2014). In addition, there is also evidence that some supernova (SN) progenitors undergo major mass ejection events shortly before exploding (e.g., Gal-Yam et al. 2007; Smith et al. 2008; Ofek et al. 2013), further altering the properties of the explosion and implying a connection between some eruptive mass-loss events and death. It is generally agreed that the effects of winds are metallicity dependent (e.g., Meynet et al. 1994; Heger et al. 2003) and the SNe requiring a very dense circumstellar medium (e.g., Schlegel 1990; Filippenko 1997) predominantly occur in lower metallicity galaxies (e.g., Stoll et al. 2011). This strongly suggests that the nature and distribution of stars undergoing impulsive mass loss will also be metallicity dependent and a full understanding requires exploring galaxies beyond the Milky Way.

Understanding the evolution of massive ($M \gtrsim 30 M_{\odot}$) stars is challenging even when mass loss is restricted to continuous winds (e.g., Fullerton et al. 2006). However, shorter, episodic eruptions, rather than steady winds, may be the dominant mass loss mechanism in the tumultuous evolutionary stages toward the end of the lives of the most massive stars (e.g., Humphreys & Davidson 1984; Smith & Owocki 2006) as they undergo periods of photospheric instabilities leading to stellar transients ($M_V \lesssim -13$) followed by rapid ($\dot{M} \gtrsim 10^{-4} M_{\odot}/\text{year}$) mass-loss in the last stages of their evolution (see Kochanek et al. 2012; Smith 2014). Deciphering the rate of these eruptions and their consequences is challenging because no true analog of η Car in mass, luminosity, energetics, mass lost and age has been found (see Smith et al. 2011; Kochanek et al. 2012), and the associated transients are significantly fainter than supernova explosions and are easily missed. These phases are as difficult to model theoretically as they are to simulate computationally.

Dense winds tend to form dust, although for hot stars the wind must be dense enough to form a pseudo-photosphere in the wind (Davidson 1987) that shields the dust formation region from the UV emission of the star (Kochanek 2011). The star will then be heavily obscured by dust for an extended period after the eruption (see, e.g., Humphreys & Davidson 1994). The Great Eruption of η Car between 1840 and 1860 is the most studied case of a stellar outburst (see, e.g., Humphreys et al. 2012). The $\sim 10 M_{\odot}$ ejecta are now seen as a dusty nebula around the star absorbing and then reradiating $\sim 90\%$ of the light in the mid-IR. This means that dusty ejecta are a powerful and long-lived signature of eruption. The emission from these dusty envelopes peaks in the mid-IR with a characteristic red color and a rising or flat spectral energy distribution (SED)

in the *Spitzer* IRAC (Fazio et al. 2004) bands.

In the Galaxy, stars with resolved shells of dust emission are easily found at $24\ \mu\text{m}$ (Wachter et al. 2010; Gvaramadze et al. 2010). The advantage of the $24\ \mu\text{m}$ band is that it can be used to identify dusty ejecta up to $10^3 - 10^4$ years after formation. A minority of these objects are very luminous stars ($L \gtrsim 10^{5.5} L_\odot$) with massive ($\sim 0.1 - 10 M_\odot$) shells (see summaries by Humphreys & Davidson 1994; Humphreys et al. 1999; Smith & Owocki 2006; Smith 2009; Vink et al. 2009). These include AG Car (Voors et al. 2000), the Pistol Star (Figer et al. 1999), G79.29+0.46 (Higgs et al. 1994), Wray 17–96 (Egan et al. 2002), and IRAS 18576+0341 (Ueta et al. 2001). These systems are significantly older ($10^3 - 10^4$ years) than η Car, which makes it difficult to use the ejecta to probe the rate or mechanism of mass-loss. Still, the abundance of Galactic shells implies that the rate of η Car-like eruptions is on the order of a modest fraction of the ccSN rate (Kochanek 2011). Their emission peaks in the shorter IRAC bands when they are relatively young ($\sim 10 - 100$ years) because the dust becomes cooler and the emission shifts to longer wavelengths as the ejected material expands (Kochanek et al. 2012). It is difficult to quantify searches for such objects in our Galaxy because it is hard to determine the distances and the survey volume because we have to look through the crowded and dusty disk of the Galaxy. Surveys of nearby galaxies are both better defined and can be used to build larger samples of younger systems whose evolution can be studied to better understand the mechanism. We previously demonstrated in Khan et al. (2010, 2011) that it is possible to identify post-eruptive massive stars in galaxies beyond the Local Group using the mid-IR excess created by warm circumstellar dust despite the crowding problems created by the limited spatial resolution of *Spitzer* at greater distances.

In Khan et al. (2013) (“Paper I” hereafter) we used archival *Spitzer* IRAC images of seven $\lesssim 4$ Mpc galaxies (closest to farthest: NGC 6822, M 33, NGC 300, NGC 2403, M 81, NGC 0247, NGC 7793) in a pilot study to search for extragalactic analogs of η Car. We found 34 candidates with flat or rising mid-IR spectral energy distributions (SEDs) and total mid-IR luminosity $L_{mIR} \gtrsim 5 \times 10^5 L_\odot$. Here, in Paper II, we characterize these sources and quantify the rate of episodic mass loss from massive stars in the last stages of evolution. First, we construct extended optical through far-IR SEDs using archival HST, 2MASS, and *Herschel* data as well as ground based data (Section 2). Then, we classify the sources as either stellar or non-stellar based on properties of the extended SEDs and model the SEDs to infer the properties of the underlying star and the obscuring circumstellar medium (Section 3). Next, we relate these properties to the observed ccSN rate of the targeted galaxies to quantify the rate of episodic mass loss in the last stages of massive star evolution (Section 4). Finally, we consider the implications of our findings for theories and observations of massive star evolution and their fates (Section 5).

2. Additional Wavelength Coverage

In this Section, we describe the details of how we obtained the photometric measurements at various wavelengths to determine the properties of the candidates from Paper I. The optical through

far-IR photometry are reported in Table 2, and the extended SEDs are shown in Figures 7 and 8.

We utilized VizieR¹ (Ochsenbein et al. 2000) to search for other observations of the candidates, in particular for WISE (Wright et al. 2010, $12\mu\text{m}$), 2MASS (Cutri et al. 2003, JHK_s), SDSS (Abazajian et al. 2009, *ugriz*) and X-ray detections. For M 33, we used the *UBVRI* images from the Massey et al. (2006) optical survey, and archival HST images of NGC 300, NGC 2403, M 81, NGC 247 and NGC 7793. Finally, we used *Herschel* PACS data to supplement the *Spitzer* measurements.

For the *Spitzer* IRAC 3.6, 4.5, 5.8 and $8\mu\text{m}$ as well as MIPS (Rieke et al. 2004) 24, 70, and $160\mu\text{m}$ data, we use the measurements reported in Paper I. For M 33, our measurements were based on IRAC data from McQuinn et al. (2007) and MIPS data from the *Spitzer Heritage Archive*². Data from the LVL survey (Dale et al. 2009) were used for NGC 300 and NGC 247, and data from the SINGS survey (Kennicutt et al. 2003) for NGC 6822, NGC 2403, and M 81.

We used the *Herschel* PACS (Poglitsch et al. 2010) 70, 100, and $160\mu\text{m}$ images available from the public *Herschel Science Archive*³. Although both MIPS and PACS cover the same far-IR wavelength range ($70 - 160\mu\text{m}$), *Herschel* has significantly higher resolution (see Figure 3). All three PACS band data were available for M 33 and NGC 7793, 70 and $160\mu\text{m}$ data were available for NGC 2403 and M 81, and 100 and $160\mu\text{m}$ data were available for NGC 300. There are no publicly available PACS images of the candidates in NGC 247. We used aperture photometry (IRAF⁴ ApPhot/Phot) with the extraction apertures and aperture corrections from Balog et al. (2013) and given in Table 1. As with our treatment of the MIPS 70 and $160\mu\text{m}$ measurements in Paper I, we treat the measurements obtained in the PACS bands as upper limits because the spatial resolution of these bands requires increasingly large apertures at longer wavelengths. For similar reasons, we also treat the WISE $12\mu\text{m}$ fluxes, where available, as upper limits.

For the optical photometry of the candidates in M 33, we used the Local Group Galaxies Survey *UBVRI* images (Massey et al. 2006). First we verified that the coordinates match with the IRAC images to within $\text{few} \times 0''.1$ and then used $1''.0$ radius extraction apertures centered on the IRAC source locations. We transformed the aperture fluxes to Vega-calibrated magnitudes using zero point offsets determined from the difference between our aperture magnitudes and calibrated magnitudes for bright stars in the Massey et al. (2006) catalog of M 33.

For the candidates in NGC 300, M 81, NGC 2403, and NGC 247, we searched the ACS Nearby Galaxy Survey (ANGST, Dalcanton et al. 2009) *B*, *V* and (where available) *I* band point source

¹<http://vizier.u-strasbg.fr/>

²<http://sha.ipac.caltech.edu/applications/Spitzer/SHA/>

³http://herschel.esac.esa.int/Science_Archive.shtml

⁴IRAF is distributed by the National Optical Astronomy Observatory, which is operated by the Association of Universities for Research in Astronomy (AURA) under cooperative agreement with the National Science Foundation.

catalogs derived using DOLPHOT (Dolphin 2000). We verified that the IRAC and HST astrometry of the NGC 300, NGC 2403 and NGC 247 images agree within (mostly) $\lesssim 0''.1$ to (in a few cases) $0''.3$. We corrected the astrometry of the M 81 HST images using the LBT images described later in this section to achieve similar astrometric accuracy. We also used the HST *I*-band photometry of M 81 from HST program GO-10250 (P.I. J. Huchra). We retrieved all publicly available archival HST images of NGC 7793 overlapping the IRAC source locations along with the associated photometry tables from the Hubble Legacy Archive⁵. The HST and *Spitzer* images have a significant (few $\times 1''.0$) astrometric mis-match, and there are too few reference stars in the HST images to adequately improve the astrometry. Therefore, we utilized the IRAF GEOXYMAP and GEOXYTRAN tasks to locally match the overlapping HST and *Spitzer* images of NGC 7793 within uncertainties of $0''.1 \sim 0''.3$.

We have variability data for the galaxies M 81 and NGC 2403 from a Large Binocular Telescope survey in the *UBVR* bands that is searching for failed supernovae (Kochanek et al. 2008), and studying supernova progenitors and impostors (Szczygieł et al. 2012), and Cepheid variables (Gerke et al. 2011). We analyzed 27 epochs of data for M 81 and 28 epochs of data for NGC 2403, spanning a 5 year period. The images were analyzed with the ISIS image subtraction package (Alard & Lupton 1998; Alard 2000) to produce light curves (see Figure 5).

3. Characterizing the Candidates

In this section, we first discuss how we classify the candidates based on their SEDs. Next, we describe the non-stellar and stellar sources. Finally, we model the SEDs of the stellar sources to determine their physical properties. Figure 7 shows the SEDs of the stellar sources with the best fit SED models over plotted and Figure 8 shows the SEDs of the non-stellar sources.

3.1. Source Classification

We classify the candidates either as stellar or non-stellar based on their photometric properties. We focus on identifying two tell-tale signatures of the SED of a luminous star obscured by warm circumstellar dust — low optical fluxes or flux-limits compared to the mid-IR luminosities and signs of the SEDs turning over between $8\ \mu\text{m}$ and $24\ \mu\text{m}$. Towards longer wavelengths, emission from warm circumstellar dust should peak between the IRAC $8\ \mu\text{m}$ and MIPS $24\ \mu\text{m}$ bands. It is almost impossible for mass lost from a single star to to both have a significant optical depth and a dust temperature cold enough to peak at wavelengths longer than $\sim 24\ \mu\text{m}$. Such systems are almost certainly star clusters with significant amounts of cold dust. Therefore, any SED that appears to have a steep slope between 8 and $24\ \mu\text{m}$ is considered to be a likely cluster, rather than a single

⁵<http://hla.stsci.edu/>

dust obscured star. Frequently, these sources are also too luminous to be a single star. At the shorter wavelengths, we expect a dusty star to have relatively lower luminosity compared to its mid-IR luminosity and redder optical colors.

We examine the HST $B - V/V$ and the $V - I/V$ color magnitude diagrams (CMDs) for each source for which HST data is available. The presence of a very red optical counterpart or the absence of a luminous star supports the existence of significant dust obscuration. On the other hand, the presence of a blue or bright optical counterpart makes it likely that the source is a star cluster, a background galaxy/AGN, or a foreground star. We first search for bright and/or red optical sources within the $0''.3$ matching radius that can be the obvious counterpart of the bright and red IRAC source. Next, if multiple bright and/or red optical matches are found, we identify the best astrometric match to the IRAC location. Finally, if no reasonable match is found, we adopt the flux of the brightest of the nearby sources as a conservative upper limit on the optical luminosity of the candidate.

To demonstrate these, we discuss the case of M 81-12 in detail. M 81-12 has a steeply rising optical and mid-IR SED (Figure 1) with two distinct peaks — one in the near-IR, between the R -band and $3.6 \mu\text{m}$, and another in the mid-IR between 8 and $24 \mu\text{m}$. Figure 4 shows the HST optical CMD for sources near the location of M 81-12. Besides the sources within the $0''.3$ matching radius, it also shows all sources within $0''.3 - 2''.0$ of the candidate using a different symbol to emphasize the absence of any other unusual nearby sources. We detect a very red ($B = 23.95$, $V = 21.98$, $I = 19.07$, $B - V \simeq 2$, $V - I \simeq 2.9$) HST counterpart with an excellent astrometric match ($< 0''.1$, Figure 2) to the IRAC position. This source is the brightest, red HST point source within $2''.0$ of the IRAC location (Figure 4) and so we define it to be the counterpart used in the SED. The LBT V and R band light curves show a variable source with the correlated irregular variability (~ 0.4 mag, Figure 5) typical of many evolved massive stars (e.g., Kourniotis et al. 2014). Based on the SED shape and the unambiguous detection of a red, variable optical counterpart, we conclude that M 81-12 is a massive, dust-obscured, single star.

In addition to Object X (M 33-1), we identified 17 additional dust obscured stars and classified 16 others as non-stellar. We left one source (N 7793-12) unclassified due to a lack of sufficient optical data (it falls on an HST/ACS chip gap). It could well be a dusty star, but we do not discuss it further.

3.2. The 18 Stars and 16 Non-stellar Sources

We identify 18 (including Object X/M 33-1) sources as dusty stars. Of these, four are in M 33 (1, 3, 4, 7), one is in NGC 300 (N 300-1), four are in NGC 2403 (2, 3, 4, 5), five are in M 81 (5, 6, 11, 12, 14), and four are in NGC 7793 (3, 9, 10, 13). None are in NGC 6822 (a low-mass, low SFR galaxy) or NGC 247 (all three candidates turned out to be non-stellar). These stars have low optical fluxes or flux limits and their SEDs turn over between $8 \mu\text{m}$ and $24 \mu\text{m}$. Moreover, M 81-

11, M 81-12 and N 2403-2 are detected as optically variable sources in the LBT monitoring data. N 2403-3 is a saturated source in the HST images, and we use the LBT flux measurements as upper limits on its optical flux. N 2403-3 and N 2403-5 are not variable in the LBT data. M 81-5 is $0''.56$ from a variable X-ray source with maximum luminosity of $2 \times 10^{38} \text{ ergs s}^{-1}$ (Liu 2011), which is consistent with the source being an X-ray binary (Remillard & McClintock 2006). N 7793-3 is also a X-ray source (Liu 2011), with a maximum X-ray luminosity of $3.9 \times 10^{37} \text{ ergs s}^{-1}$ and is classified as an HMXB by Mineo et al. (2012).

There are 16 candidates whose SEDs indicate that they are not self-obscured stars. Five sources in M 33 (2, 5, 6, 8, 9) have SEDs that nearly monotonically rise from the optical to $24 \mu\text{m}$, unambiguously indicating the presence of cold dust associated with star clusters. As we discussed in Paper I, it is unlikely for an ultra-compact star cluster to host both evolved massive stars and significant amounts of intra-cluster dust. Eight sources cannot be dust obscured stars given their very high optical luminosities: N 2403-1 (likely a foreground star), M 81-7, M 81-10, N 247-3 (likely a foreground star, optical magnitudes from GSC2.2 2001), N 7793-4, N 7793-8, N 7793-11, and N 7793-14. The three observed with the LBT, M 81-7, M 81-10 and N 2403-1, are not variable. We consider three more sources as most likely non-stellar due to reasons that are unique in each case —

- N 247-1 is located far from the plane of its edge-on host and is unlikely to be associated with the host.
- N 7793-1 is located at the edge of its host galaxy and the PACS far-IR flux limits are significantly lower than those of the sources that we classified as obscured stars, indicating an absence of the diffuse emission commonly associated with star forming regions.
- N 7793-6 has an SED that can conceivably be produced by a hot star with significant circumstellar material, although the near-IR peak seems too narrow. However, a close inspection of the HST image shows that this source is in a dense star-forming region with significant diffuse light indicating the presence of intra-cluster dust. None of the sources in the HST image are a good astrometric match to the IRAC location. It is more likely, in this case, that warm intercluster dust is producing the mid-IR flux excess. The optical fluxes adopted here are those of the most luminous HST source within a larger matching radius of $0''.5$.

In Paper I, we anticipated that further analysis would show that most, if not all, of the candidates are in fact non-stellar sources. Based on the expected surface density of extragalactic contaminants, of the 46 initial candidates we estimated that all but 6 ± 6 are background galaxies/AGN with 11 already being identified as such. Here we find that 18 (including Object X) of the candidates are dusty massive stars and very few of the other sources are background galaxies. We do not presently have an explanation for the fewer than expected background sources in the targeted fields.

3.3. SED Modeling

We fit the SEDs of the 18 self-obscured stars using DUSTY (Ivezic & Elitzur 1997; Ivezic et al. 1999; Elitzur & Ivezić 2001) to model radiation transfer through a spherical dusty medium surrounding a star and Figure 7 shows the best fit models. We estimate the properties of a black-body source obscured by a surrounding dusty shell that would produce the best fit to the observed SED (see Figure 6 for an example). We considered models with either graphitic or silicate (Draine & Lee 1984) dust. We distributed the dust in a shell with a $\rho \propto 1/r^2$ density distribution. The models are defined by the stellar luminosity (L_*), stellar temperature (T_*), the total (absorption plus scattering) V -band optical depth (τ_V), the dust temperature at the inner edge of the dust distribution (T_d), and the shell thickness $\zeta = R_{out}/R_{in}$. The exact value of ζ has little effect on the results, and after a series of experiments with $1 < \zeta < 10$, we fixed $\zeta = 4$ for the final results. We embedded DUSTY inside a Markov Chain Monte Carlo (MCMC) driver to fit each SED by varying T_* , τ_V , and T_d . We limit T_* to a maximum value of 30,000 K to exclude unrealistic temperature regimes.

The parameters of the best fit model determine the radius of the inner edge of the dust distribution (R_{in}). The mass of the shell is

$$M_e = \frac{4\pi R_{in}^2 \tau_V}{\kappa_V} \quad (1)$$

where we simply scale the mass for a V band dust opacity of $\kappa_V = 100 \kappa_{100} \text{ cm}^2 \text{ g}^{-1}$ and the result can be rescaled for other choices as $M_e \propto \kappa_V^{-1}$. Despite using a finite width shell, we focus on R_{in} because it is well-constrained while R_{out} (or ζ) is not. We can also estimate an age for the shell as

$$t_e = \frac{R_{in}}{v_e} \quad (2)$$

where we scale the results to $v_e = 100 v_{e100} \text{ km s}^{-1}$.

For a comparison sample, we followed the same procedures for the SEDs of three well-studied dust obscured stars: η Car (Humphreys & Davidson 1994); the Galactic OH/IR star IRC+10420 (Jones et al. 1993; Humphreys et al. 1997; Tiffany et al. 2010); and M 33’s Variable A, which had a brief period of high mass loss leading to dust obscuration over the last ~ 50 years (Hubble & Sandage 1953; Humphreys et al. 1987, 2006). We use the same SEDs for these stars as in Khan et al. (2013). In Table 3, we report χ^2 , τ_V , T_d , T_* , R_{in} , L_* , M_e (Equation 1), and t_e (Equation 2) for the best fit models for these three sources as well as the newly identified stars. The stellar luminosities required for both dust types are mutually consistent because the optically thick dust shell acts as a calorimeter. However, because the stars are heavily obscured and we have limited optical/near-IR SEDs, the stellar temperatures generally are not well constrained. In some cases, for different dust types, equally good models can be obtained for either a hot ($> 25000 \text{ K}$, such as a LBV in quiescence) or a relatively cooler ($< 10000 \text{ K}$, such as a LBV in outburst) star. Indeed, for many of our 18 sources, the best fit is near the fixed upper limit of $T_* = 30000 \text{ K}$. To address this issue, we also tabulated the models on a grid of three fixed stellar temperatures, $T_* = 5000 \text{ K}, 7500 \text{ K}, 20000 \text{ K}$, for each dust type. The resulting best fit parameters are reported in Tables 4 and 5.

Figure 9 shows the integrated luminosities of the newly identified self-obscured stars described in Section 3.2 as a function of M_e for the best fit graphitic models of each source. Object X, IRC+10420, M 33 Var A, and η Car are shown for comparison. Figure 10 shows the same quantities, but for various dust models and temperature assumptions. It is apparent from Figure 10 and Tables 3, 4 and 5 that the integrated luminosity and ejecta mass estimates are robust to these uncertainties. The exceptions are N 2403-4 and N 7793-3. Without any optical or near-IR data, many of the models of N 7793-3 are unstable so we simply drop it. The only models having a luminosity in significant excess of $10^6 L_\odot$ are some of the fixed temperature models of N 2403-4. These models have a poor goodness of fit and can be ignored.

One check on our selection methods is to examine the distribution of shell radii. Crudely, we can see a shell until it either becomes optically thin or too cold, so the probability distribution of a shell’s radius assuming a constant expansion velocity is

$$\frac{dN}{dR_{in}} = \frac{1}{R_{max}} = \text{constant} \quad (3)$$

for $R_{in} < R_{max}$. An ensemble of shells with similar R_{max} should then show this distribution. Figure 11 shows the cumulative histogram (excluding N 7793-3) of the inner shell radii (R_{in}). The curves show the expected distribution where we simply normalized to the point where $F(< R_{in}) \simeq 0.5$. The agreement shows that our sample should be relatively complete up to $R_{max} \simeq 10^{16.5-10^{17}}$ cm which corresponds to a maximum age of

$$t_{max} \simeq 300 v_{e100}^{-1} \text{ years.} \quad (4)$$

Figure 12 shows the age ($t_e = R_{in}/v_{e100}^{-1}$) of the shells as a function of M_e . We also show lines corresponding to optical depths of $\tau_V = 1, 10, 100$. As expected, we see no sources with very low or high optical depths, as we should have trouble finding sources with $\tau_V < 1$ due to a lack of mid-IR emission and $\tau_V \gtrsim 100$ due to the dust photosphere being too cold (peak emission in the far-IR). Indeed, most of the dusty stars have $1 < \tau_V < 10$ and none has $\tau_V > 100$. The large t_e estimate for η Car when scaled by v_{e100} is due to its unusually large ejecta velocities ($\sim 600 \text{ km s}^{-1}$ along the long axis (Cox et al. 1995; Smith 2006) compared to typical LBV shells ($\sim 50 - 100 \text{ km s}^{-1}$, Tiffany et al. 2010).

4. Implications

The advantage of surveying external galaxies with a significant supernova rate is that we can translate our results into estimates of abundances and rates. We scale our rates using the observed supernova rate of $R_{SN} = 0.15 \text{ year}^{-1}$ ($0.05 < R_{SN} < 0.35$ at 90% confidence). As we discussed in Paper I, this is significantly higher than standard star formation rate estimates for these galaxies, but the SN rate is directly proportional to the massive star formation rate rather than an indirect indicator, and similar discrepancies, although not as dramatic, have been noted in other contexts

(e.g., Horiuchi et al. 2011). In this section we first outline how we will estimate rates, and then we discuss the constraints on analogs of η Car and the implications of our sample of luminous dusty stars.

We are comparing a sample of $N_{SN} = 3$ supernovae observed over $t_{SN} = 20$ years to a sample of N_c candidate stars which are detectable by our selection procedures for a time t_d . In Paper I we used DUSTY to model the detection of expanding dusty shells and found that a good estimate for the detection time period was

$$t_d = t_w + 66 \left(\frac{100 \text{ km s}^{-1}}{v_e} \right) \left(\frac{L_*}{10^6 L_\odot} \right)^{0.82} \left(\frac{M_e}{M_\odot} \right)^{0.043} \text{ years} \quad (5)$$

for shells with masses in the range $-1 \leq \log M_e/M_\odot \leq 1$ around stars of luminosity $5.5 \leq \log L_*/L_\odot \leq 6.5$ where t_w is the duration of the “wind” phase and the second term is an estimate of how long the shell will be detected after the heavy mass loss phase ends. The principle uncertainty lies in the choice of the velocity, v_e . If the rate of events in the sample is R_e , then we expect to find $N_e = R_e t_d$ candidates.

The transient rate in a sample of galaxies is less interesting than comparing the rate to the supernova rate. Let f_e be the fraction of massive ($M_{ZAMS} > 8 M_\odot$) stars that create the transients, where $f_e = (M_C/8M_\odot)^{-1.35}$ if we assume a Salpeter IMF (Kennicutt 1998), that all stars more massive than $8M_\odot$ become supernovae and that all stars more massive than M_C cause the transients. If each star undergoes an average of N_e eruptions, then the rate of transients is related to the rate of supernovae by $R_e = N_e f_e R_{SN} = F_e R_{SN}$. The interesting quantity to constrain is $F_e = N_e f_e$ rather than R_e . Poisson statistics provide constraints on the rates, where $P(D|R) \propto (Rt)^N \exp(-Rt)$ for N events observed over a time period t . This means that the probability of the rates given the data is

$$P(R_{SN}, R_e|D) \propto P(R_{SN})P(R_e)(R_{SN}t_{SN})^3 (R_e t_d)^{N_c} \exp(-R_{SN}t_{SN} - R_e t_d) \quad (6)$$

where $P(R_{SN})$ and $P(R_e)$ are priors on the rates which we will assume to be uniform and we have set $N_{SN} = 3$. If we now change variables to compute F_e and marginalize over the unknown supernova rate, we find that the probability distribution for the ratio of the rates is

$$P(F_e|D) \propto F_e^{N_c} (F_e t_d + t_{SN})^{-5-N_c} \quad (7)$$

with the standard normalization that $\int P(F_e|D) dF_e \equiv 1$. For our estimates of F_e we present either 90% confidence upper limits or the value corresponding to the median probability and symmetric 90% probability confidence regions. Note that the probability distribution really just depends on the product $F_e t_d$, so the results for any given estimate of t_d are easily rescaled.

4.1. No η Car Analog Is Found

It is immediately obvious from Figure 9 that none of the sources we identified closely resemble η Car. Their typical luminosities of $10^{5.7 \pm 0.2} L_\odot$ correspond to $\sim 40 M_\odot$ stars (Maeder 1981;

Maeder & Meynet 1987, 1988; Stothers & Chin 1996; Meynet et al. 1994) rather than the higher masses usually associated with LBV outbursts. Since we identify a significant population of fainter stars, this is unlikely to be a selection effect, and we conclude that these galaxies contain no analogs of η Car.

There are two ways we can interpret the result. First, we can ignore the existence of η Car, and set $N_c = 0$. Alternatively, we can acknowledge the existence of η Car, in which case $N_c = 1$, since η Car passes our selection criterion and mid-IR surveys of our Galaxy for objects as luminous as η Car are probably complete. For the first case, the 90% confidence upper limit is $F_e < 0.077t_{d200}^{-1}$ where the period over which such systems can be detected is scaled to $t_d = 200t_{d200}$ years. For the second case, where we include η Car, we find that $F_e = 0.046t_{d200}^{-1}$ with $0.0083 < F_e t_{d200} < 0.19$ at 90% confidence. In either case, the rate of transients comparable to η Car is a small fraction of the supernova rate.

Stars as massive as η Car are also rare, representing only $f_e = 0.02$ to 0.04 of all massive stars for a mass range from $70/100M_\odot$ to $200M_\odot$. If every sufficiently massive star had one eruption, the results including η Car correspond to a minimum mass of $M_C = 65M_\odot$ ($26M_\odot < M_C < 138M_\odot$). If every star has an average of two eruptions, the mass limits rise to $M_C = 94M_\odot$ ($42M_\odot < M_C < 162M_\odot$). Similarly the upper limit from ignoring the existence of η Car corresponds to $M_C > 48M_\odot$ for an average of one eruption or $M_C > 72M_\odot$ for an average of two. Kochanek (2011) estimated that the abundance of lower optical depth shells found at $24\mu\text{m}$ around massive stars in the Galaxy was roughly consistent with all stars more massive than $M_C = 40M_\odot$ having an average of two eruptions, corresponding to $F_e \simeq 0.2$, which is consistent with the present results, but close to the upper limits.

4.2. An Emerging Class of Dust Obscured Stars

All the newly identified stars have luminosities within a narrow range of $\log L/L_\odot \simeq 5.5$ - 6.0 (see Figure 10), which roughly corresponds to initial stellar masses of $M_{ZAMS} \simeq 25$ - $60M_\odot$ (see Section 4 of de Jager 1998, and references therein). Local examples of evolved stars in this luminosity range are the Yellow Hypergiants (YHGs) such as IRC+10420, ρ Cas and HR 8752 (de Jager & Nieuwenhuijzen 1997; Smith & Owocki 2006), many of which are also partially obscured by dust ejecta. There is no means of cleanly surveying the Galaxy for these objects and they are so rare that samples in the Galaxy and the Magellanic Clouds do not provide good statistics for their abundances, life times or total mass loss. Our well-defined sample of likely extragalactic analogs provides a means of addressing some of these questions.

If we assume these objects are similar to stars like IRC+10420, their expansion velocities will be more like 50 km/s than the 100 km/s of the typical LBV shell. Hence, it seems more appropriate to scale the results to $t_d = 500t_{d500}$ years. This also matches the estimated age of the phase of dusty mass loss by IRC+10420 (Tiffany et al. 2010). With 18 candidates, this detection period

then leads to a median estimate that $F_e = 0.20t_{d500}^{-1}$ with $0.086 < F_e t_{d500} < 0.55$. If we associate these with the mass range from 25 to $60M_\odot$, they represent a fraction of $f_e \simeq 0.15$ of massive stars, so the average number of episodes per star, $N_e = F_e/f_e \simeq 1.3t_{d500}^{-1}$ with a possible range of $0.58 < N_e t_{d500} < 3.7$, although this does not include the uncertainties in f_e

Figure 9 shows that the median mass causing the obscuration is $M_e \sim 0.5M_\odot$. The total mass lost in all the eruptions is then of order $N_e M_e$, which would be of order $0.3\text{--}1.9t_{d500}^{-1}M_\odot$. This implies that the periods of optically thick (dusty) mass loss cannot dominate the overall mass loss of the star. To make the mass lost in these phases dominate either requires that we have grossly overestimated t_d , or that the mass range of the stars is much narrower. A related point is that these phases represent a negligible fraction of the post-main-sequence life times of the stars, at most lasting a few thousand years.

5. Conclusions

In our survey, we have found no true analogs of η Car. This implies that the rate of Great Eruption-like events is of order $F_e = 0.046t_{d200}^{-1}$ ($0.0083 < F_e t_{d200} < 0.19$) of the ccSN rate, which is roughly consistent with each $M \gtrsim 70M_\odot$ star undergoing 1 or 2 such outbursts in its lifetime. This is scaled by an estimated detection period of order $t_d = 200t_{d200}$ years. We do identify a significant population of lower luminosity dusty stars that are likely similar to IRC+10420. Stars enter this phase at the rate $F_e = 0.20t_{d500}^{-1}$ ($0.086 < F_e t_{d500} < 0.55$) compared to the ccSN rate and for a detection period of $t_d = 500t_{d500}$ years. Here the detection period is assumed longer because the expansion velocities are likely slower. This rate is comparable to having all stars with $25 < M < 60M_\odot$ undergoing such a phase once or twice.

If the estimated detection periods and mass ranges are roughly correct, and our completeness is relatively high, there are two interesting implications for both populations. First, these high optical depth phases represent a negligible fraction of the post-main sequence lifetimes of these stars, at most lasting a few thousand years. This implies that these events have to be associated with special periods in the evolution of the stars. The number of such events a star experiences is also small, one or two, not ten or twenty. Second, while a significant amount of mass is lost in the eruptions, they cannot be a dominant contribution to mass loss. For these high mass stars, standard models (e.g., Maeder 1981; Maeder & Meynet 1987, 1988; Stothers & Chin 1996; Meynet et al. 1994) typically strip the stars of their hydrogen envelopes and beyond, implying total mass losses of all but the last $5\text{--}10M_\odot$. The median mass loss in Figure 9 is $M_e \sim 0.5M_\odot$ and if every star underwent two eruptions, the typical total would be $N_e M_e \sim M_\odot$. Clearly there are some examples that require significantly larger M_e , but we simply do not find enough heavily obscured stars for this phase to represent more than a modest fraction of the total mass loss ($\sim 10\%$ not $\sim 50\%$).

For the stars similar to IRC+10420, this is consistent with the picture that the photospheres of blue-ward evolving Red Super Giants (RSGs) with $\log(L_*/L_\odot) = 5.6 \sim 6.0$ and $T_{star} \simeq 7000\text{--}$

12500 K, become moderately unstable, leading to periods of lower effective temperature and enhanced mass loss as the stars try to evolve into a “prohibited” region of the HR diagram that de Jager & Nieuwenhuijzen (1997), de Jager (1998) and Nieuwenhuijzen & de Jager (2000) termed the “yellow void”. In this phase, the stars lose enough mass to evolve into a hotter, less massive star on the blue side of the HR diagram. This is also the luminosity regime of the “bistability jump” in wind speeds driven by opacity changes which Smith et al. (2004) hypothesizes can explain the absence of LBVs and the existence of YHG with high mass loss rates and dust formation (Vink et al. 2009) in this luminosity range. In fact, Humphreys et al. (2002) propose that IRC+10420, which is identified by our selection criterion, is such a star. While these arguments supply a unique, short-lived evolutionary phase, there may be problems with the absolute scale of the mass loss, since estimates are that IRC+10420 started with a mass of $\sim 40M_{\odot}$ and has lost all but $6 \sim 15M_{\odot}$ (Nieuwenhuijzen & de Jager 2000).

The only other similarly unique phase in the lives of these stars is the final post-carbon ignition phase. There are now many examples of stars which have had outbursts shortly before exploding as supernovae (e.g., Pastorello et al. 2007; Mauerhan et al. 2013; Prieto et al. 2013; Pastorello et al. 2013; Ofek et al. 2013) and superluminous supernovae that are most easily explained by surrounding the star with a large amount of previously ejected mass (Smith & McCray 2007; Gal-Yam et al. 2007; Smith et al. 2008; Kozłowski et al. 2010; Ofek et al. 2013). Powering these supernovae requires mass ejected in the last years to decades of the stellar life (e.g., Chevalier & Fransson 1994; Chugai & Danziger 2003; Smith 2009; Moriya et al. 2014). and it seems natural to associate these events with the mass ejections of LBVs like η Car (e.g., Smith & McCray 2007; Gal-Yam & Leonard 2009). The statistical properties and masses of either of the classes of dusty stars we discuss are well-matched to the statistical requirements for explaining these interaction powered supernovae if the instability is associated with the onset of carbon burning (see Kochanek 2011). If there is only one eruption mechanism, it must be associated with a relatively long period like carbon burning (thousands of years) rather than the shorter, later nuclear burning phases, because we observe many systems like η Car that have survived far longer than these final phases last. If the mechanism for producing the ejecta around the superluminous supernovae is associated with nuclear burning phases beyond carbon, then we must have second eruption mechanism to explain η Car or other still older LBVs surrounded by massive dusty shells. If there indeed are two mass loss mechanisms — one commencing $\gtrsim 10^3$ years from core-collapse and the other occurring in the ~ 1 year prior to core-collapse — then the self-obscured stars identified in this work may very well be experiencing the earlier of these two mechanisms. Otherwise, in a larger sample to ~ 100 such stars, one should be exploding as a ccSN every ~ 10 years.

The dusty stars can be further characterized by their variability, which will help to follow the evolution of the dust. For the optically brighter examples, it may be possible to spectroscopically determine the stellar temperatures, although detailed study may only become possible with the James Webb Space Telescope (*JWST*). It is relatively easy to expand our survey to additional galaxies. For very luminous sources like η Car analogs this is probably feasible to distance of 10 Mpc,

while for the lower luminosity IRC+10420 analogs this is likely only feasible at the distances of the most distant galaxies in our sample (~ 4 Mpc). Larger galaxy samples are needed not only to increase the sample of dusty luminous stars (and hopefully find a true η Car analog!), but also to have a sample with a larger number of supernovae, or equivalently a higher star formation rate. Our estimate of the abundance of IRC+10420 analogs is limited by the small number of ccSN (3) in our sample more than by the number of dusty stars (18) identified. Finally, while we have shown that surveys for the stars are feasible using archival Spitzer data, JWST will be a far more powerful probe of these stars. The HST-like resolution (Gardner et al. 2006) will be enormously useful to either greatly reduce the problem of confusion or to greatly expand the survey volume. Far more important will be the ability to carry out the survey at $24\mu\text{m}$, which will increase the time over which dusty shells can be identified from hundreds of years to thousands of years, greatly improving the statistics and our ability to survey the long term evolution of these systems and the relationship between stellar eruptions and supernovae.

We thank Hendrik Linz for helping us analyze the Herschel PACS data and John Beacom for numerous productive discussions. We extend our gratitude to the SINGS Legacy Survey and LVL Survey for making their data publicly available. This research has made use of observations made with the NASA/ESA Hubble Space Telescope, and obtained from the Hubble Legacy Archive, which is a collaboration between the Space Telescope Science Institute (STScI/NASA), the Space Telescope European Coordinating Facility (ST-ECF/ESA) and the Canadian Astronomy Data Centre (CADC/NRC/CSA). RK and KZS are supported in part by NSF grant AST-1108687.

REFERENCES

- Abazajian, K. N. et al. 2009, *ApJS*, 182, 543
- Alard, C. 2000, *A&AS*, 144, 363
- Alard, C. & Lupton, R. H. 1998, *ApJ*, 503, 325
- Balog, Z. et al. 2013, *Experimental Astronomy*
- Bionta, R. M., Blewitt, G., Bratton, C. B., Casper, D., & Ciocio, A. 1987, *Physical Review Letters*, 58, 1494
- Chevalier, R. A. & Fransson, C. 1994, *ApJ*, 420, 268
- Chugai, N. N. & Danziger, I. J. 2003, *Astronomy Letters*, 29, 649
- Cox, P., Mezger, P. G., Sievers, A., Najarro, F., Bronfman, L., Kreysa, E., & Haslam, G. 1995, *A&A*, 297, 168
- Cutri, R. M. et al. 2003, *2MASS All Sky Catalog of point sources.*, ed. R. M. Cutri et al.

- Dalcanton, J. J. et al. 2009, *ApJS*, 183, 67
- Dale, D. A. et al. 2009, *ApJ*, 703, 517
- Davidson, K. 1987, *ApJ*, 317, 760
- de Jager, C. 1998, *A&A Rev.*, 8, 145
- de Jager, C. & Nieuwenhuijzen, H. 1997, *MNRAS*, 290, L50
- Dolphin, A. E. 2000, *PASP*, 112, 1383
- Draine, B. T. & Lee, H. M. 1984, *ApJ*, 285, 89
- Egan, M. P., Clark, J. S., Mizuno, D. R., Carey, S. J., Steele, I. A., & Price, S. D. 2002, *ApJ*, 572, 288
- Elitzur, M. & Ivezić, Ž. 2001, *MNRAS*, 327, 403
- Fazio, G. G. et al. 2004, *ApJS*, 154, 10
- Figer, D. F., McLean, I. S., & Morris, M. 1999, *ApJ*, 514, 202
- Filippenko, A. V. 1997, *ARA&A*, 35, 309
- Fullerton, A. W., Massa, D. L., & Prinja, R. K. 2006, *ApJ*, 637, 1025
- Gal-Yam, A. et al. 2007, *ApJ*, 656, 372
- Gal-Yam, A., & Leonard, D. C. 2009, *Nature*, 458, 865
- Gardner, J. P. et al. 2006, *Space Sci. Rev.*, 123, 485
- Gerke, J. R., Kochanek, C. S., Prieto, J. L., Stanek, K. Z., & Macri, L. M. 2011, *ApJ*, 743, 176
- GSC2.2. 2001, *VizieR Online Data Catalog*, 1271, 0
- Gvaramadze, V. V., Kniazev, A. Y., & Fabrika, S. 2010, *MNRAS*, 405, 1047
- Heger, A., Fryer, C. L., Woosley, S. E., Langer, N., & Hartmann, D. H. 2003, *ApJ*, 591, 288
- Higgs, L. A., Wendker, H. J., & Landecker, T. L. 1994, *A&A*, 291, 295
- Horiuchi, S., Beacom, J. F., Kochanek, C. S., Prieto, J. L., Stanek, K. Z., & Thompson, T. A. 2011, *ApJ*, 738, 154
- Hubble, E. & Sandage, A. 1953, *ApJ*, 118, 353
- . 1984, *Science*, 223, 243

- Humphreys, R. M. & Davidson, K. 1994, *PASP*, 106, 1025
- Humphreys, R. M., Jones, T. J., & Gehrz, R. D. 1987, *AJ*, 94, 315
- Humphreys, R. M., Davidson, K., & Smith, N. 1999, *PASP*, 111, 1124
- . 2002, *AJ*, 124, 1026
- Humphreys, R. M. et al. 1997, *AJ*, 114, 2778
- Humphreys, R. M., Davidson, K., Jones, T. J., Pogge, R. W., Grammer, S. H., Prieto, J. L., & Pritchard, T. A. 2012, *ApJ*, 760, 93
- . 2006, *AJ*, 131, 2105
- Ivezic, Z. & Elitzur, M. 1997, *MNRAS*, 287, 799
- Ivezic, Z., Nenkova, M., & Elitzur, M. 1999, *ArXiv Astrophysics e-prints*, 9910475
- Jones, T. J. et al. 1993, *ApJ*, 411, 323
- Kennicutt, Jr., R. C. et al. 2003, *PASP*, 115, 928
- Khan, R., Stanek, K. Z., & Kochanek, C. S. 2013, *ApJ*, 767, 52
- Khan, R., Stanek, K. Z., Kochanek, C. S., & Bonanos, A. Z. 2011, *ApJ*, 732, 43
- Khan, R., Stanek, K. Z., Prieto, J. L., Kochanek, C. S., Thompson, T. A., & Beacom, J. F. 2010, *ApJ*, 715, 1094
- Kennicutt, Jr., R. C. 1998, *ApJ*, 498, 541
- Kochanek, C. S. 2011, *ApJ*, 743, 73
- Kochanek, C. S., Szczygiel, D. M., & Stanek, K. Z. 2012, *ApJ*, 758, 142
- Kochanek, C. S. et al. 2008, *ApJ*, 684, 1336
- Kourniotis, M. et al. 2014, *A&A*, 562, A125
- Kozlowski, S., Kochanek, C. S., Stern, D., Prieto, J. L., & Stanek, K. Z. 2010, *Central Bureau Electronic Telegrams*, 2392, 1
- Liu, J. 2011, *ApJS*, 192, 10
- Maeder, A. 1981, *A&A*, 101, 385
- Maeder, A. & Meynet, G. 1987, *A&A*, 182, 243
- . 1988, *A&AS*, 76, 411

- Massey, P., Olsen, K. A. G., Hodge, P. W., Strong, S. B., Jacoby, G. H., Schlingman, W., & Smith, R. C. 2006, *AJ*, 131, 2478
- Mauerhan, J. C. et al. 2013, *MNRAS*, 430, 1801
- McQuinn, K. B. W. et al. 2007, *ApJ*, 664, 850
- Meynet, G., Maeder, A., Schaller, G., Schaerer, D., & Charbonnel, C. 1994, *A&AS*, 103, 97
- Mineo, S., Gilfanov, M., & Sunyaev, R. 2012, *MNRAS*, 419, 2095
- Moriya, T. J., Maeda, K., Taddia, F., Sollerman, J., Blinnikov, S. I., & Sorokina, E. I. 2014, *MNRAS*, 439, 2917
- Nieuwenhuijzen, H. & de Jager, C. 2000, *A&A*, 353, 163
- Ochsenbein, F., Bauer, P., & Marcout, J. 2000, *A&AS*, 143, 23
- Ofek, E. O. et al. 2013, *Nature*, 494, 65
- . 2014a, *ApJ*, 789, 104
- . 2014b, *ApJ*, 781, 42
- Ott, C. D. 2009, *Classical and Quantum Gravity*, 26, 204015
- Pastorello, A. et al. 2007, *Nature*, 447, 829
- . 2013, *ApJ*, 767, 1
- Poglitsch, A. et al. 2010, *A&A*, 518, L2
- Prieto, J. L., Brimacombe, J., Drake, A. J., & Howerton, S. 2013, *ApJ*, 763, L27
- Remillard, R. A. & McClintock, J. E. 2006, *ARA&A*, 44, 49
- Rieke, G. H. et al. 2004, *ApJS*, 154, 25
- Robinson, G., Hyland, A. R., & Thomas, J. A. 1973, *MNRAS*, 161, 281
- Schlegel, E. M. 1990, *MNRAS*, 244, 269
- Smartt, S. J. 2009, *ARA&A*, 47, 63
- Smith, N. 2009, *ArXiv e-prints*, 0906.2204
- . 2014, *ArXiv e-prints*
- Smith, N. & McCray, R. 2007, *ApJ*, 671, L17

- Smith, N. & Owocki, S. P. 2006, *ApJ*, 645, L45
- Smith, N., Vink, J. S., & de Koter, A. 2004, *ApJ*, 615, 475
- Smith, N. 2006, *ApJ*, 644, 1151
- Smith, N. et al. 2008, *ApJ*, 686, 467
- Smith, N., Li, W., Silverman, J. M., Ganeshalingam, M., & Filippenko, A. V. 2011, *MNRAS*, 415, 773
- Stanek, K. Z. et al. 2003, *ApJ*, 591, L17
- Stoll, R. et al. 2011, *ApJ*, 730, 34
- Stothers, R. B. & Chin, C.-W. 1996, *ApJ*, 468, 842
- Szczygiel, D. M., Gerke, J. R., Kochanek, C. S., & Stanek, K. Z. 2012, *ApJ*, 747, 23
- Tiffany, C., Humphreys, R. M., Jones, T. J., & Davidson, K. 2010, *AJ*, 140, 339
- Ueta, T., Meixner, M., Dayal, A., Deutsch, L. K., Fazio, G. G., Hora, J. L., & Hoffmann, W. F. 2001, *ApJ*, 548, 1020
- Vink, J. S., Davies, B., Harries, T. J., Oudmaijer, R. D., & Walborn, N. R. 2009, *A&A*, 505, 743
- Voors, R. H. M. et al. 2000, *A&A*, 356, 501
- Wachter, S., Mauerhan, J. C., Van Dyk, S. D., Hoard, D. W., Kafka, S., & Morris, P. W. 2010, *AJ*, 139, 2330
- Woods, P. M. et al. 2011, *MNRAS*, 411, 1597
- Wright, E. L. et al. 2010, *AJ*, 140, 1868

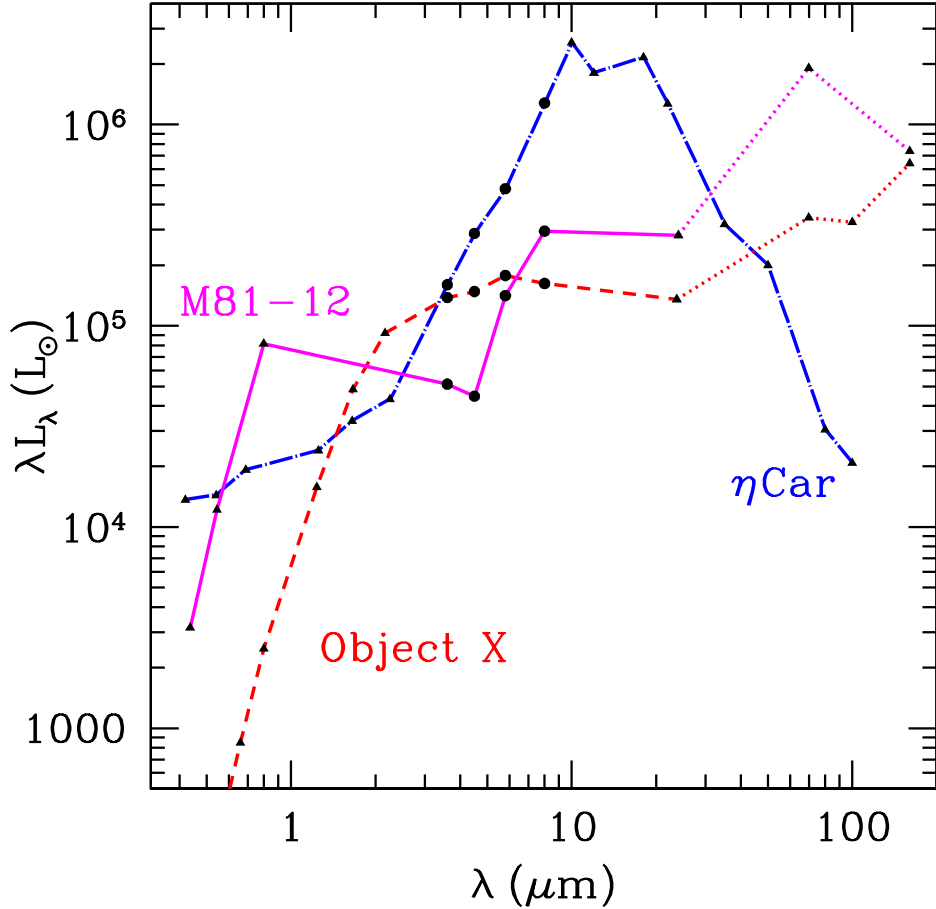


Fig. 1.— The spectral energy distributions (SEDs) of the dust-obscured massive star η Car (dash-dot line, e.g., Robinson et al. 1973; Humphreys & Davidson 1994), “Object X” in M33 (dashed line; Khan et al. 2011), and an obscured star in M81 that we identify in this paper (M81-12, solid line). All these stars have SEDs that are flat or rising in the *Spitzer* IRAC 3.6, 4.5, 5.8 and 8.0 μm bands (marked here by solid circles). The three shortest wavelength data-points of the M81-12 SED are from HST *BVI* images. The 24 μm measurements of both Object X and M81-12 are from *Spitzer* MIPS while the dotted segments of their SEDs show the *Herschel* PACS 70, 100, and 160 μm upper limits.

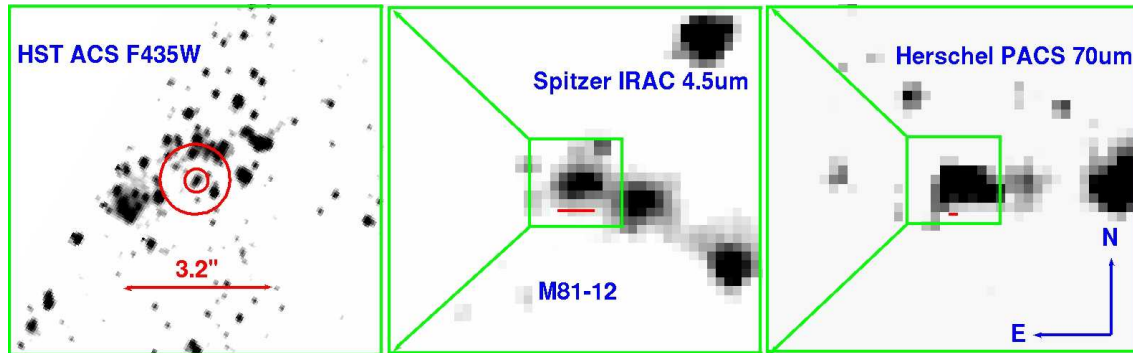


Fig. 2.— The *Hubble*, *Spitzer*, and *Herschel* images of the region around M 81-12. In the left panel, the radii of the circles are $0''.25$ (5 ACS pixels) and $1''.43$ (IRAC $4.5\ \mu\text{m}$ PSF FWHM), and the source at the position of the smaller circle in the left panel is the brightest red point source on the CMD (Figure 4, *left* panel). The red line in each panel is the size of a PACS pixel ($3''.2$).

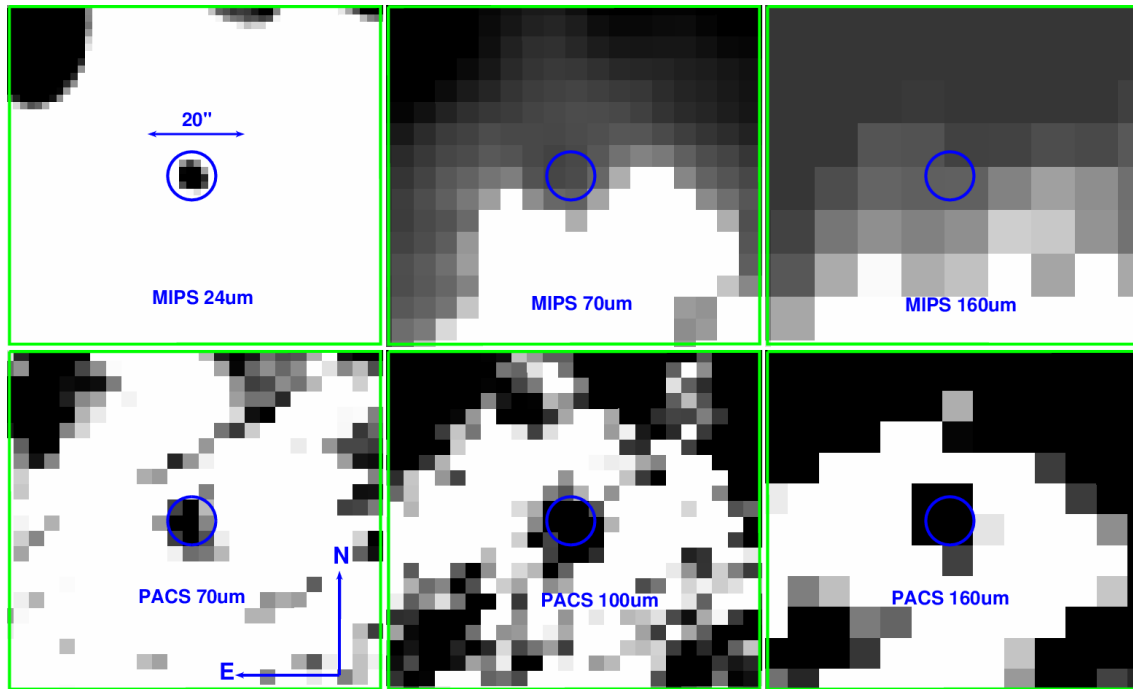


Fig. 3.— The *Spitzer* MIPS 24, 70 and 160 μm (top row) and *Herschel* PACS 70, 100 and 160 μm (bottom row) images of the region around the object N7793-9. The higher resolution of the PACS images helps us set tighter limits on the far-IR emission from the candidates.

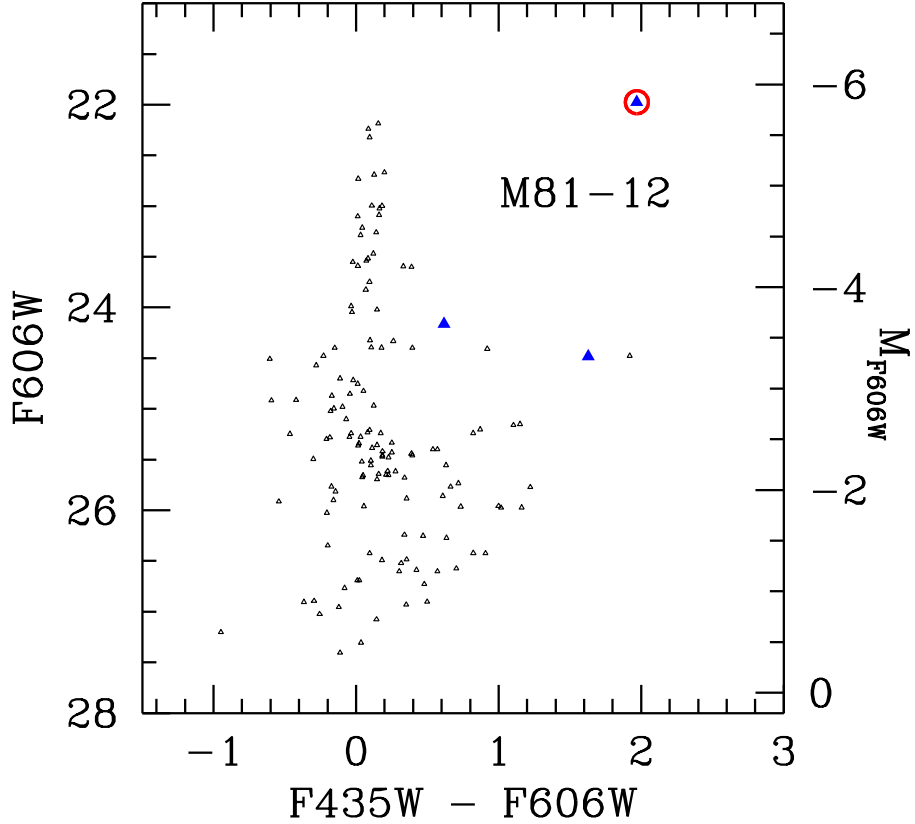


Fig. 4.— The $F606W$ (V) vs. $F435W - F606W$ ($B - V$) color magnitude diagram (CMD) for all HST point sources around M81-12. The three large solid triangles denote sources located with the $0''.3$ matching radius. The small open triangles show all other sources within a larger $2''.0$ radius to emphasize the absence of any other remarkable sources nearby. The circle marks the source at the position of the smaller circle in the left panel of Figure 2, which is the brightest red point source on the CMD. The excellent ($< 0''.1$) astrometric match and the prior that very red sources are rare confirms that this source is the optical counterpart of the mid-IR bright red *Spitzer* source.

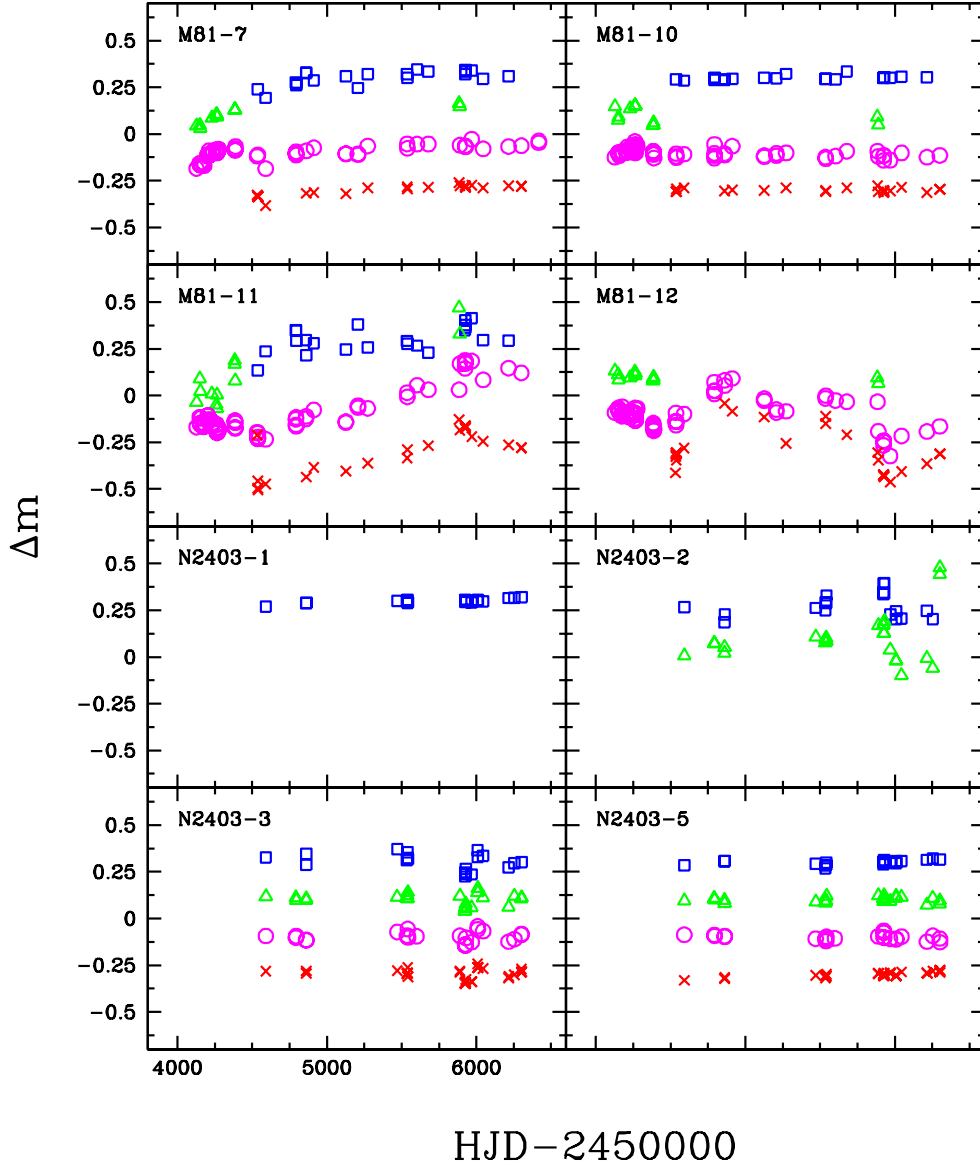


Fig. 5.— The differential light curves of some of the candidates in M81 and NGC 2403 obtained from the Large Binocular Telescope. The data spans the period from March 2008 to January 2013. The U (squares), B (triangles), V (circles), R (crosses) differential magnitudes are offset by +0.3, +0.1, -0.1, -0.3 mag for clarity.

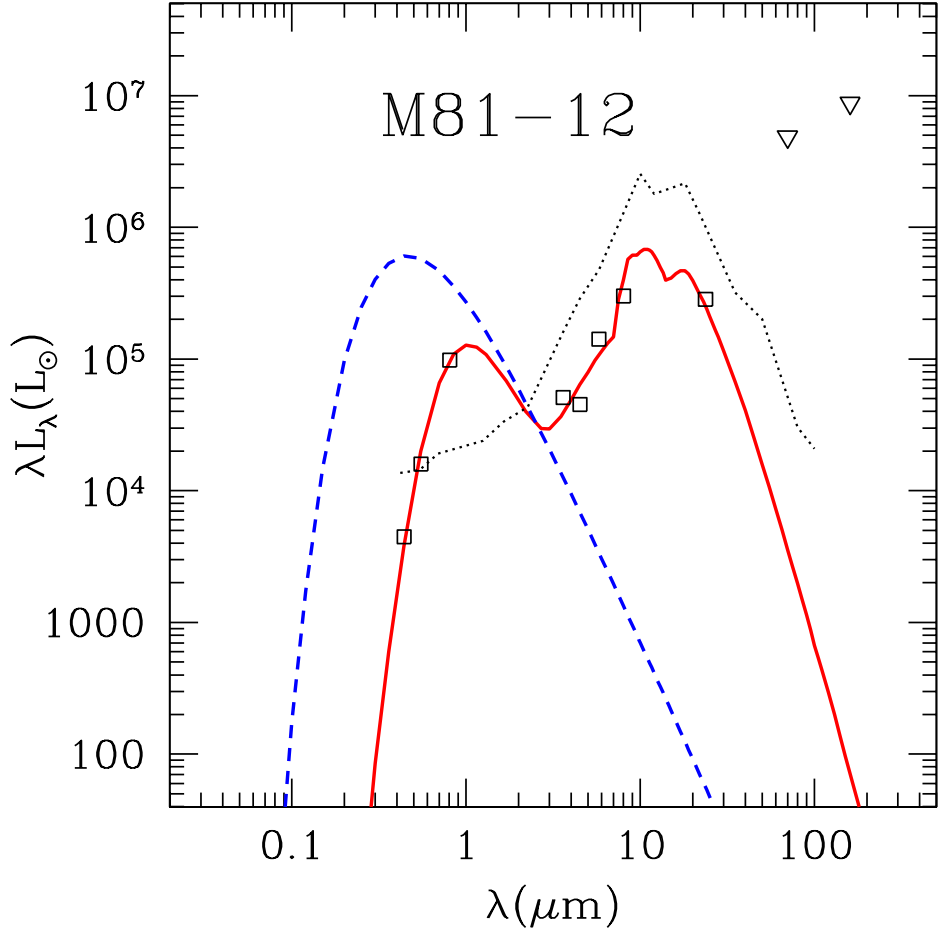


Fig. 6.— The best fit model (solid line) of the observed SED (squares and triangles, the latter show flux upper limits) of M81-12 and the SED of the underlying, unobscured star (dashed line), as compared to η Car (dotted line). The best fit is for a $L_* \simeq 10^{5.9} L_\odot$, $T_* \simeq 7900$ K star obscured by $\tau_V \simeq 8$, $T_d \simeq 530$ K silicate dust shell at $R_{in} = 10^{16.1}$ cm.

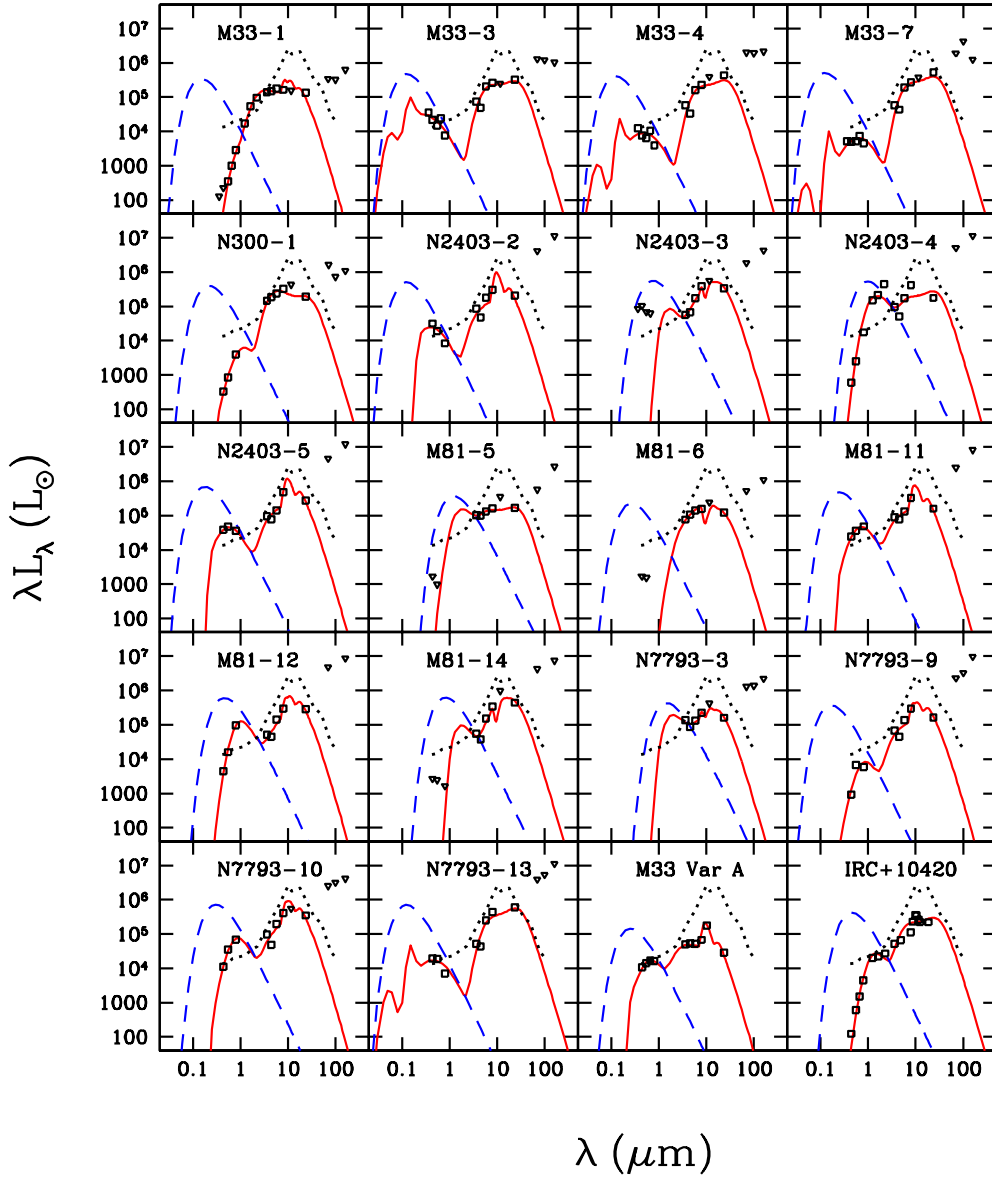


Fig. 7.— Same as Figure 6, but showing all the obscured stars that we identified as compared to M33 Var A, *IRC* + 10420, and η Car. The solid line shows the best fit model of the observed SED, and the dashed line shows the SED of the underlying, unobscured star. M33 Var A and *IRC*+10420 are shown on separate panel while η Car is shown on every panel (dotted line).

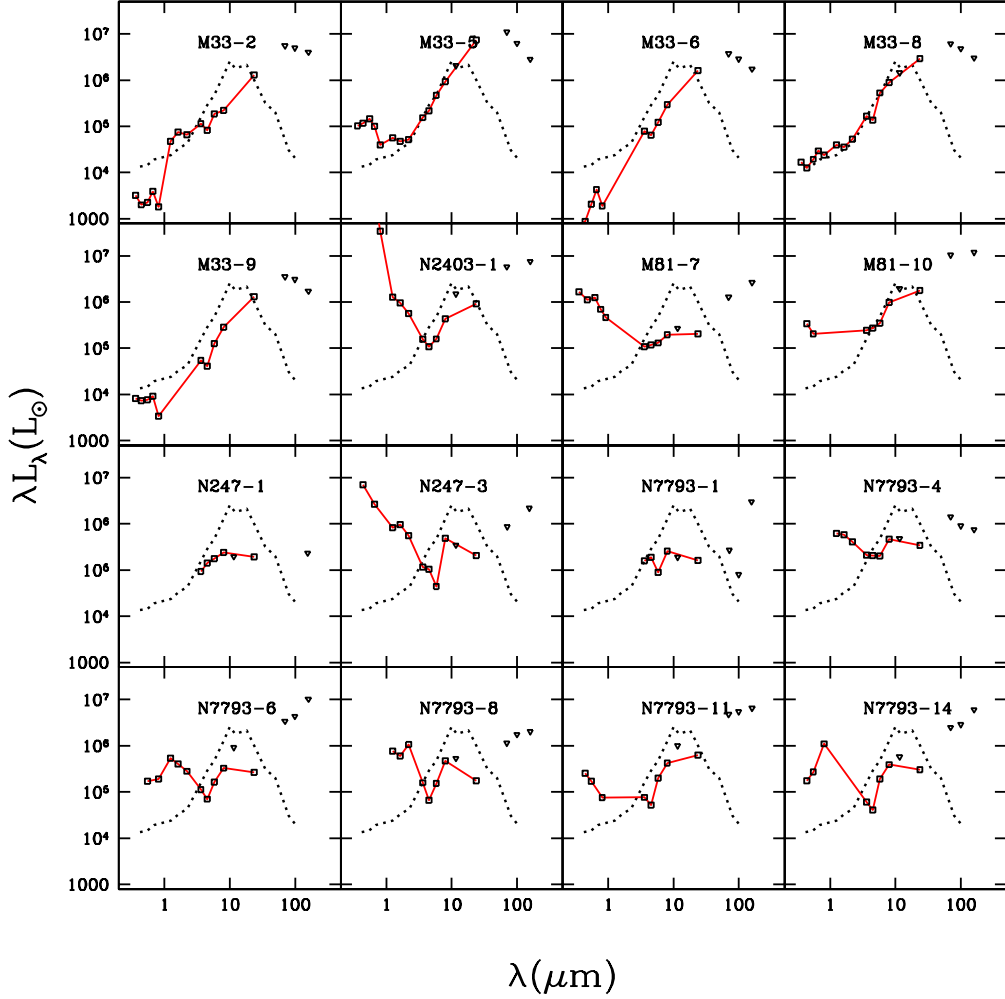


Fig. 8.— The SEDs of the 16 candidates that we concluded are not stars (points and solid lines) as compared to η Car (dotted line).

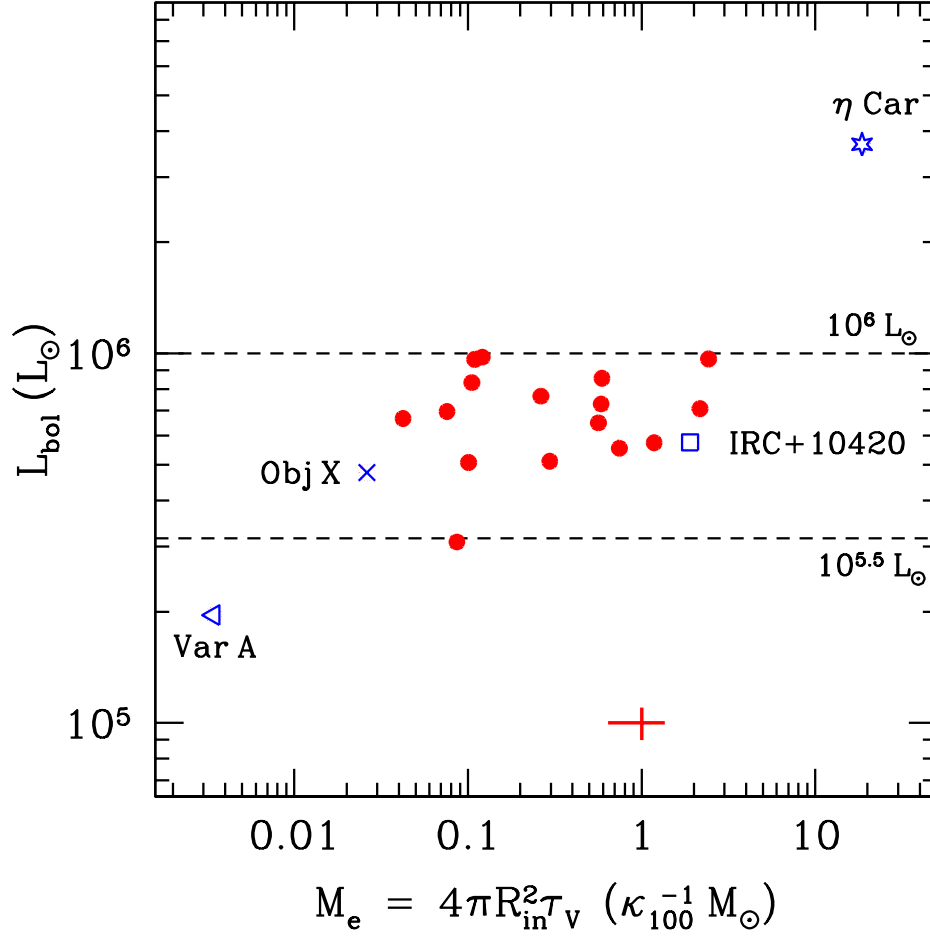


Fig. 9.— Luminosities of the obscured stars as a function of the estimated ejecta mass determined from the best fit model for each SED. The dashed lines enclose the luminosity range $\log(L/L_{sun}) \simeq 5.5 - 6.0$. We do not show N 7793-3 for which we have no optical or near-IR data. *IRC + 10420* (square), M33 Var A (triangle), and η Car (star symbol) are shown for comparison. The error bar corresponds to the typical 1σ uncertainties on L_{bol} ($\pm 10\%$) and M_e ($\pm 35\%$) of the best SED fit models.

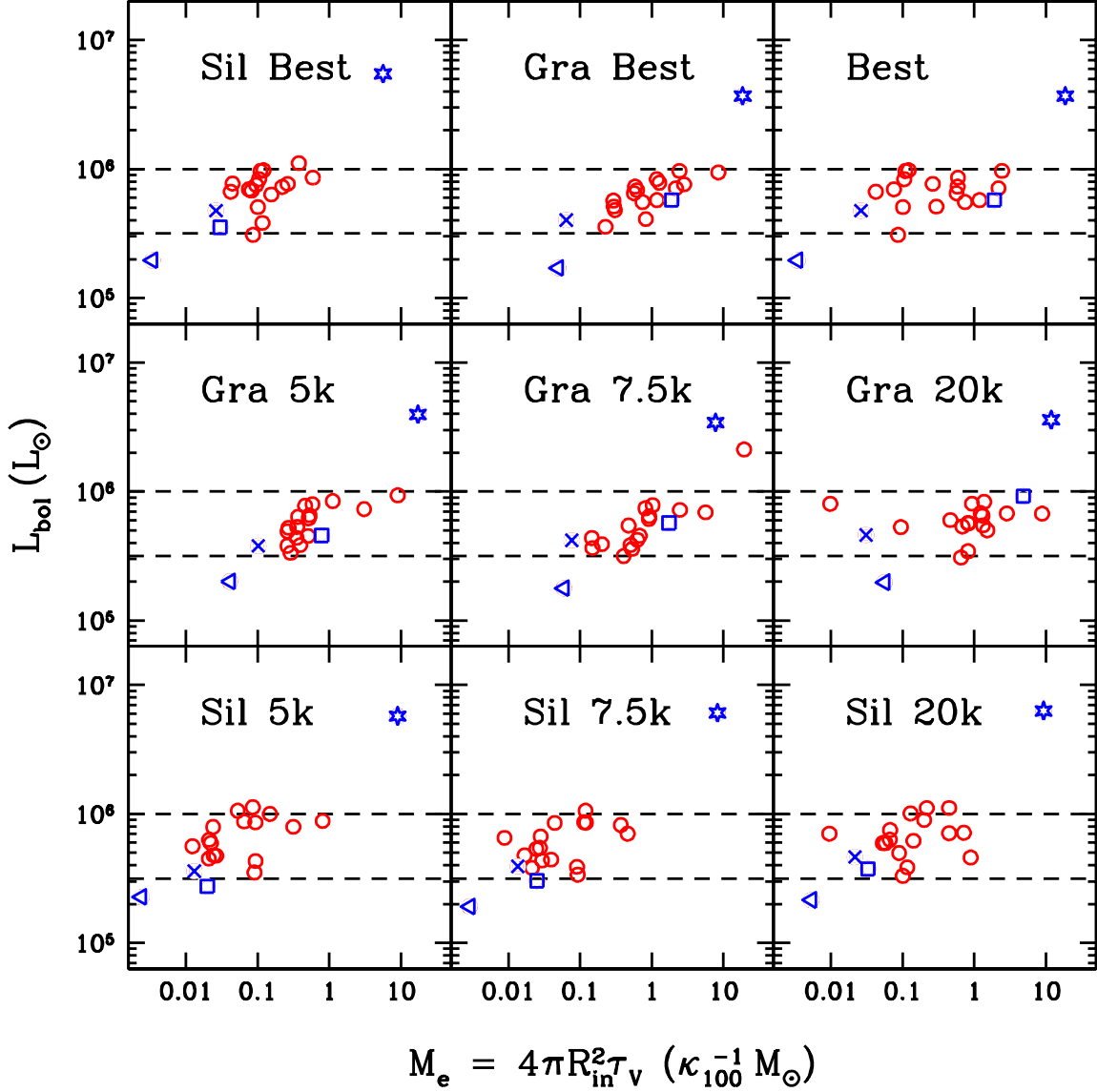


Fig. 10.— Same as Figure 9, but for different dust types and temperature assumptions. The top row shows the best silicate (left), graphitic (center), and the better of the two (right, same as Figure 9) models. The middle and bottom rows show the best fit models for graphitic and silicate dust at fixed stellar temperatures of 5000 K, 7500 K and 20000 K. The only higher luminosity case in the fixed temperature model panels is N 2403-4, for which the best fit models have significantly smaller χ^2 and lower luminosities for both dust types.

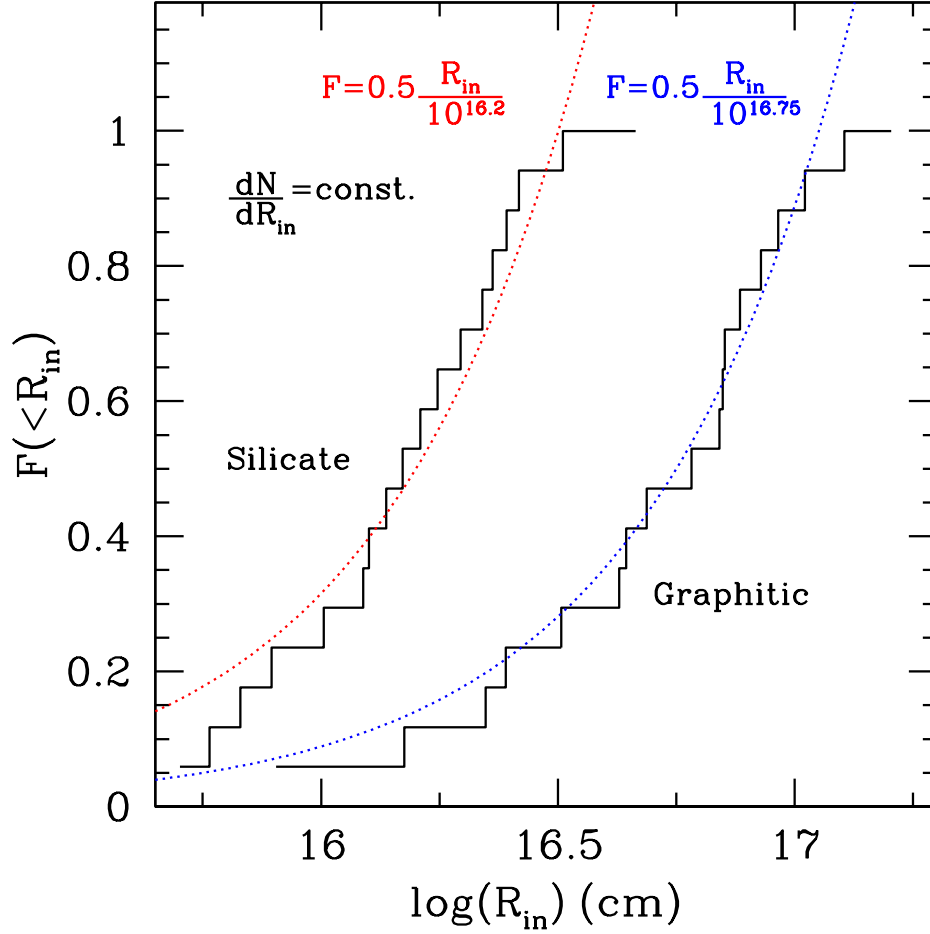


Fig. 11.— Cumulative histograms of the dust shell radius R_{in} for the newly identified stars excluding N 7793-3. The dotted lines, normalized to the point where $F(< R_{in}) = 0.5$, shows the distribution expected for shells in uniform expansion observed at a random time.

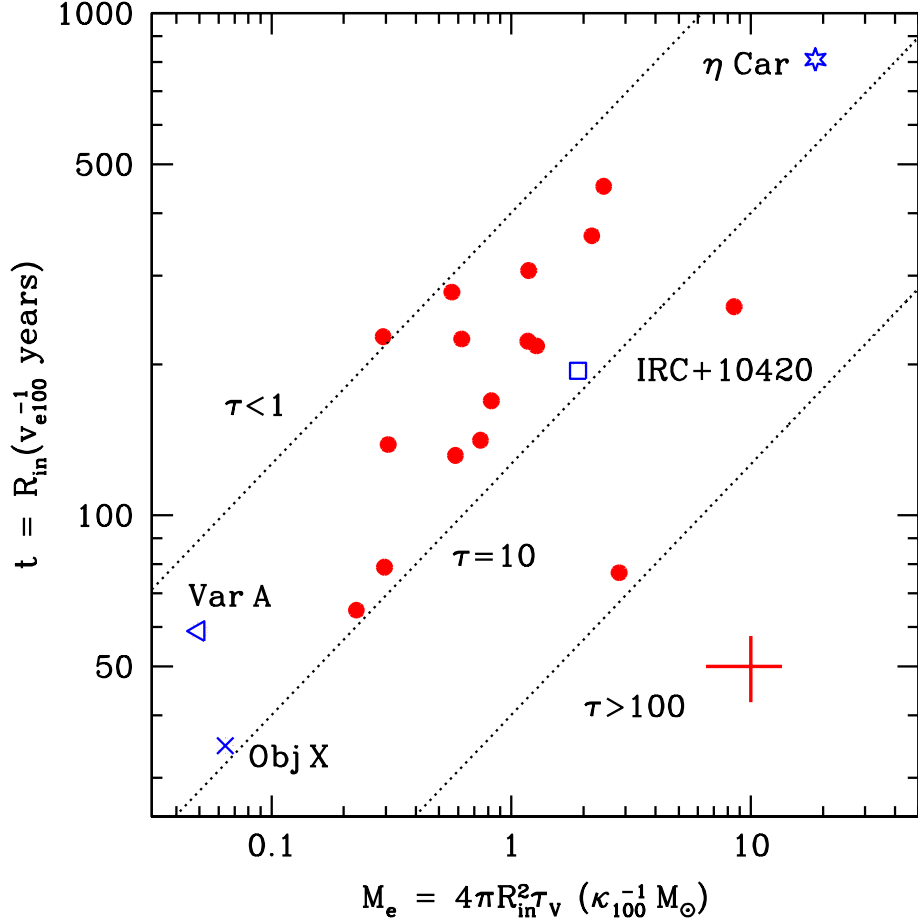


Fig. 12.— Elapsed time $t = R_{in}v_{e100}^{-1}$ as a function of the estimated ejecta mass M_e for the best fit graphitic models. The mass and radius are scaled to $\kappa_V = 100 \kappa_{100} \text{ cm}^2 \text{ gm}^{-1}$ and $v_e = 100 v_{e100} \text{ km s}^{-1}$, and can be rescaled as $t \propto v_e^{-1}$ and $M_e \propto \kappa_V^{-1}$. The error bar shows the typical 1σ uncertainties on t ($\pm 15\%$) and M_e ($\pm 35\%$) of the best SED fit models. The three dotted lines correspond to optical depths $\tau_V = 1, 10$ and 100 . We should have trouble finding sources with $\tau_V < 1$ due to lack of mid-IR emission and $\tau_V \gtrsim 100$ due to the dust photosphere being too cold (peak emission in far-IR). The large t estimate for η Car when scaled by v_{e100} is due to the anomalously large ejecta velocities ($\sim 600 \text{ km s}^{-1}$ along the long axis (Cox et al. 1995; Smith 2006) compared to typical LBV shells ($\sim 50 \text{ km s}^{-1}$, Tiffany et al. 2010).

Table 1: PACS Aperture Definitions

| Band (μm) | Pixel Scale | R_{ap} | R_{in} | R_{out} | Ap. Corr. |
|------------------------|-------------|----------|----------|-----------|--------------------|
| 70 μm | 3''2 | 6''4 | 60''8 | 70''4 | 0.72 ⁻¹ |
| 100 μm | 3''2 | 6''4 | 60''8 | 70''4 | 0.69 ⁻¹ |
| 160 μm | 6''4 | 12''8 | 121''6 | 140''8 | 0.78 ⁻¹ |

Table 2: Multi-Wavelength Photometry^a

| ID | <i>U</i> | <i>B</i> | <i>V</i> | <i>R</i> | <i>I</i> | <i>J</i> | <i>H</i> | <i>K_s</i> | [3.6] | [4.5] | [5.8] | [8.0] | [12] | [24] | [70] | [100] | [160] |
|-----------------------|----------|----------|----------|----------|----------|----------|----------|----------------------|-------|-------|-------|-------|-------|------|-------------------|-------|--------------------|
| M 33 – 1 | < 24.1 | < 24.3 | 23.15 | 21.61 | 19.99 | 17.07 | 15.04 | 13.60 | 11.73 | 10.92 | 9.97 | 9.08 | 7.85 | 5.71 | 278.1 | 377.1 | 1181 |
| M 33 – 2 | 20.61 | 21.84 | 21.14 | 20.13 | 20.48 | 15.96 | 14.68 | 14.02 | 11.93 | 11.56 | 9.91 | 8.75 | ... | 3.27 | 4503 | 5791 | 7501 |
| M 33 – 3 | 18.00 | 19.26 | 19.10 | 18.16 | 18.92 | ... | ... | ... | 12.39 | 12.11 | 9.80 | 8.56 | 7.35 | 4.75 | 1064 | 1407 | 1916 |
| M 33 – 4 | 19.14 | 20.37 | 20.00 | 19.08 | 19.62 | ... | ... | ... | 12.66 | 12.54 | 10.07 | 8.71 | 6.84 | 4.44 | 1648 | 2249 | 4017 |
| M 33 – 5 | 16.84 | 17.43 | 16.62 | 16.62 | 17.12 | 15.77 | 15.17 | 14.28 | 11.61 | 10.51 | 8.91 | 7.20 | 5.06 | 1.38 | 8959 | 7250 | 5237 |
| M 33 – 6 | 22.17 | 22.73 | 21.23 | 20.04 | 20.42 | ... | ... | ... | 12.33 | 11.83 | 10.37 | 8.43 | ... | 3.03 | 3026 | 3338 | 3250 |
| M 33 – 7 | 20.09 | 20.84 | 20.25 | 19.45 | 19.48 | ... | ... | ... | 12.68 | 12.26 | 9.89 | 8.52 | 6.91 | 4.22 | 1548 | 4955 | 2329 |
| M 33 – 8 | 18.81 | 19.85 | 18.81 | 17.94 | 17.68 | 16.15 | 15.49 | 14.25 | 11.52 | 11.01 | 8.78 | 7.25 | 5.44 | 2.38 | 4955 | 5581 | 5607 |
| M 33 – 9 | 19.60 | 20.42 | 19.81 | 19.22 | 19.80 | ... | ... | ... | 12.74 | 12.31 | 10.33 | 8.48 | ... | 3.24 | 2875 | 3590 | 3206 |
| N 300 – 1 | ... | 25.23 | 23.68 | ... | 21.13 | ... | ... | ... | 13.22 | 12.23 | 11.22 | 9.91 | 8.33 | 6.90 | 0.96 ^F | 200.1 | 475 |
| N 2403 – 1 | ... | 9.23 | ... | 11.04 | 12.28 | 14.89 | 14.42 | 14.21 | 14.10 | 13.79 | 12.60 | 10.54 | 7.93 | 6.15 | 465.4 | ... | 1385 |
| N 2403 – 2 | ... | 21.3 | 21.3 | ... | 21.3 | ... | ... | ... | 14.77 | 14.67 | 12.47 | 10.91 | ... | 7.77 | 330.4 | ... | 2045 |
| N 2403 – 3 | < 19.5 | < 20.0 | < 19.9 | < 19.6 | ... | ... | ... | ... | 15.22 | 14.28 | 12.51 | 10.65 | 8.98 | 7.22 | 148.4 | ... | 790.5 |
| N 2403 – 4 | ... | 25.6 | 23.5 | ... | 20.5 | 17.21 | 16.05 | 14.45 | 14.65 | 14.60 | 12.50 | 10.59 | ... | 7.94 | 408.8 | ... | 2100 |
| N 2403 – 5 | ... | 21.1 | 20.3 | ... | 19.7 | ... | ... | ... | 14.64 | 14.13 | 12.74 | 10.41 | ... | 7.45 | 369.4 | ... | 2230 |
| M 81 – 5 | ... | < 25 | < 25 | ... | ... | ... | ... | ... | 14.93 | 14.25 | 13.16 | 11.99 | 9.86 | 8.36 | 32.7 | ... | 346.7 |
| M 81 – 6 | ... | < 25 | < 24.5 | ... | ... | ... | ... | ... | 15.26 | 14.18 | 13.09 | 12.03 | 10.26 | 8.72 | 30.1 | ... | 142.1 |
| M 81 – 7 ^b | 17.55 | 17.57 | 17.09 | 17.46 | 17.66 | ... | ... | ... | 14.89 | 14.07 | 13.19 | 11.78 | 10.15 | 8.15 | 72.4 | ... | 343.8 |
| M 81 – 10 | ... | 19.25 | 19.20 | ... | ... | ... | ... | ... | 14.00 | 13.15 | 12.13 | 10.02 | 8.00 | 5.80 | 589.2 | ... | 1534 |
| M 81 – 11 | ... | 22.10 | 21.10 | ... | 19.83 | ... | ... | ... | 15.09 | 14.50 | 13.17 | 11.22 | ... | 8.42 | 142.3 | ... | 1067 |
| M 81 – 12 | ... | 23.95 | 21.98 | ... | 19.07 | ... | ... | ... | 15.70 | 15.10 | 13.10 | 11.31 | ... | 7.79 | 275.6 | ... | 1141 |
| M 81 – 14 | ... | < 24.5 | < 24 | ... | < 23.5 | ... | ... | ... | 15.61 | 15.30 | 13.01 | 8.74 | ... | 7.31 | 243.1 | ... | 966.3 |
| N 247 – 1 | ... | ... | ... | ... | ... | ... | ... | ... | 15.04 | 13.86 | 12.87 | 11.56 | 10.51 | 8.23 | ... | ... | 1.84 ^F |
| N 247 – 3 | ... | 15.73 | ... | 15.87 | ... | 15.73 | 14.79 | 14.58 | 14.80 | 14.20 | 14.38 | 10.80 | 9.88 | 8.14 | 2.98 ^F | ... | –0.59 ^F |
| N 7793 – 1 | ... | ... | ... | ... | ... | ... | ... | ... | 14.72 | 13.79 | 13.85 | 11.74 | 10.79 | 8.65 | 4.49 ^F | 5.142 | –0.69 ^F |
| N 7793 – 3 | ... | ... | ... | ... | ... | ... | ... | ... | 14.89 | 14.64 | 13.42 | 11.89 | 9.92 | 8.67 | 57.9 | 89.61 | 228.2 |
| N 7793 – 4 | ... | ... | ... | ... | ... | 16.30 | 15.59 | 15.17 | 14.40 | 13.70 | 12.97 | 11.08 | 9.77 | 7.85 | 63.7 | 58.18 | 76.83 |
| N 7793 – 6 | ... | ... | 19.5 | ... | 18.5 | 16.45 | 15.98 | 15.58 | 15.09 | 14.88 | 13.19 | 11.47 | 9.09 | 8.12 | 152.1 | 267.7 | 1044 |
| N 7793 – 8 | ... | ... | ... | ... | ... | 16.07 | 15.56 | 14.14 | 14.72 | 14.93 | 13.27 | 11.08 | 9.67 | 8.58 | 50.9 | 111.8 | 207.2 |
| N 7793 – 9 | ... | 25.7 | 23.0 | ... | 22.3 | ... | ... | ... | 15.65 | 15.38 | 13.40 | 11.57 | ... | 8.64 | 103.6 | 210.1 | 989.7 |
| N 7793 – 10 | ... | 23.0 | 21.2 | ... | 19.6 | ... | ... | ... | 15.26 | 15.29 | 13.00 | 11.23 | 9.62 | 7.83 | 114.0 | 205.1 | 426.1 |
| N 7793 – 11 | ... | 19.6 | 19.5 | ... | 19.5 | ... | ... | ... | 15.51 | 15.20 | 12.98 | 11.20 | 8.98 | 7.20 | 213.5 | 349.9 | 669.1 |
| N 7793 – 12 | ... | ... | ... | ... | ... | ... | ... | ... | 15.89 | 15.37 | 13.58 | 11.57 | ... | 7.84 | 63.3 | 121.0 | 666.7 |
| N 7793 – 13 | ... | 22.4 | 21.9 | ... | 22.1 | ... | ... | ... | 15.92 | 15.39 | 12.72 | 11.15 | ... | 7.25 | 176 | 345.4 | 1141 |
| N 7793 – 14 | ... | 20.0 | 19.0 | ... | 16.6 | ... | ... | ... | 15.77 | 15.47 | 13.02 | 11.28 | 9.58 | 7.97 | 111.4 | 185.2 | 614.8 |

^aOptical, near-IR, *Spitzer* IRAC 3.6 – 8.0 μm , WISE 12 μm , and *Spitzer* MIPS 24, 70, and 160 μm measurements in apparent magnitudes. *Herschel* PACS 70, 100 and 160 μm measurements in flux (mJy). WISE, MIPS, and PACS measurements are always treated as upper limits.

^bOptical measurement are SDSS *ugriz* magnitudes, not *UBVRI*.

^c*Spitzer* MIPS 70 μm and 160 μm apparent magnitudes, not *Herschel* flux (mJy).

Table 3: Best Fit Models

| ID | <i>Graphitic</i> | | | | | | | | <i>Silicate</i> | | | | | | | |
|-------------|------------------|----------|--------------|--------------|------------------------|-----------------------------|------------------------|------------------|-----------------|----------|--------------|--------------|------------------------|-----------------------------|------------------------|------------------|
| | χ^2 | τ_V | T_d (K) | T_* (K) | $\log(R_{in})$ (cm) | $\log L_*$ (L_\odot) | M_e (M_\odot) | t_e (years) | χ^2 | τ_V | T_d (K) | T_* (K) | $\log(R_{in})$ (cm) | $\log L_*$ (L_\odot) | M_e (M_\odot) | t_e (years) |
| M 33 – 1 | 46 | 8.46 | 708 | 6749 | 16.04 | 5.60 | 0.026 | 34.79 | 18 | 10.70 | 1218 | 24602 | 15.80 | 5.68 | 0.064 | 19.8 |
| M 33 – 3 | 34 | 1.16 | 416 | 29927 | 16.94 | 5.81 | 0.096 | 278.5 | 55 | 2.63 | 649 | 29955 | 16.38 | 5.88 | 0.565 | 76.21 |
| M 33 – 4 | 47 | 2.00 | 390 | 29977 | 16.99 | 5.76 | 0.156 | 307.3 | 75 | 3.88 | 599 | 29991 | 16.40 | 5.80 | 1.182 | 80.14 |
| M 33 – 7 | 29 | 2.67 | 381 | 29931 | 17.06 | 5.85 | 0.222 | 360.5 | 57 | 4.79 | 599 | 29973 | 16.43 | 5.86 | 2.170 | 85.98 |
| N 300 – 1 | 4 | 5.97 | 506 | 17129 | 16.65 | 5.74 | 0.083 | 141.1 | 8 | 8.57 | 959 | 28956 | 16.09 | 5.83 | 0.744 | 39.24 |
| N 2403 – 2 | 30 | 0.90 | 440 | 29988 | 16.85 | 5.76 | 0.076 | 227 | 26 | 2.56 | 676 | 29942 | 16.34 | 5.84 | 0.292 | 68.79 |
| N 2403 – 3 | 8 | 76.36 | 455 | 2533 | 16.38 | 5.88 | 0.263 | 76.89 | 2 | 25.27 | 499 | 4981 | 16.11 | 5.88 | 2.821 | 40.8 |
| N 2403 – 4 | 100 | 5.39 | 398 | 3790 | 16.62 | 5.86 | 0.045 | 131.7 | 146 | 10.00 | 568 | 4545 | 15.93 | 5.89 | 0.585 | 26.78 |
| N 2403 – 5 | 27 | 1.97 | 429 | 16146 | 16.85 | 5.84 | 0.109 | 224.6 | 5 | 3.56 | 662 | 20750 | 16.34 | 5.98 | 0.621 | 70.06 |
| M 81 – 5 | 1 | 7.60 | 428 | 3050 | 16.40 | 5.71 | 0.117 | 78.89 | 2 | 35.00 | 1117 | 29778 | 15.86 | 5.58 | 0.296 | 23.14 |
| M 81 – 6 | 0.9 | 8.61 | 504 | 4897 | 16.31 | 5.55 | 0.086 | 64.76 | 0.5 | 46.97 | 985 | 13885 | 15.73 | 5.49 | 0.226 | 17.15 |
| M 81 – 11 | 17 | 2.56 | 463 | 10825 | 16.64 | 5.68 | 0.042 | 138.4 | 3 | 4.54 | 746 | 15015 | 16.09 | 5.82 | 0.307 | 38.59 |
| M 81 – 12 | 12 | 4.31 | 365 | 5548 | 16.84 | 5.89 | 0.105 | 217.5 | 10 | 7.84 | 529 | 7910 | 16.16 | 5.92 | 1.275 | 46.34 |
| M 81 – 14 | 14 | 20.08 | 341 | 4839 | 16.91 | 5.97 | 0.591 | 260.4 | 8 | 29.47 | 416 | 4528 | 16.25 | 5.93 | 8.513 | 56.65 |
| N 7793 – 3 | ... | ... | ... | ... | ... | ... | ... | ... | ... | ... | ... | ... | ... | ... | ... | ... |
| N 7793 – 9 | 46 | 4.61 | 432 | 14632 | 16.73 | 5.61 | 0.101 | 169.2 | 27 | 7.04 | 713 | 22072 | 16.18 | 5.70 | 0.825 | 47.86 |
| N 7793 – 10 | 32 | 3.80 | 396 | 7406 | 16.85 | 5.92 | 0.121 | 222.3 | 25 | 6.36 | 609 | 12175 | 16.24 | 5.99 | 1.174 | 55.18 |
| N 7793 – 13 | 32 | 1.90 | 369 | 29943 | 17.15 | 5.99 | 0.377 | 452.2 | 42 | 4.01 | 546 | 29989 | 16.59 | 6.05 | 2.431 | 122.6 |
| IRC+10420 | 222 | 8.06 | 399 | 8157 | 16.79 | 5.76 | 0.030 | 194.2 | 240 | 11.86 | 835 | 11780 | 15.80 | 5.55 | 1.900 | 20.17 |
| M 33 Var A | 43 | 2.29 | 536 | 11741 | 16.27 | 5.23 | 0.003 | 58.86 | 8 | 4.11 | 1046 | 14549 | 15.56 | 5.29 | 0.050 | 11.54 |
| η Car | 490 | 4.55 | 361 | 18134 | 17.41 | 6.57 | 5.611 | 809 | 853 | 7.99 | 468 | 26164 | 17.02 | 6.74 | 18.615 | 335.1 |

Table 4: Best Fit Models for Graphitic Dust and Fixed Temperature

| ID | $T_* = 5000 K$ | | | | | $T_* = 7500 K$ | | | | | $T_* = 20000 K$ | | | | |
|-------------|----------------|--------------|------------------------|-----------------------------|------------------------|----------------|--------------|------------------------|-----------------------------|------------------------|-----------------|--------------|------------------------|-----------------------------|------------------------|
| | τ_V | T_d (K) | $\log(R_{in})$ (cm) | $\log L_*$ (L_\odot) | M_e (M_\odot) | τ_V | T_d (K) | $\log(R_{in})$ (cm) | $\log L_*$ (L_\odot) | M_e (M_\odot) | τ_V | T_d (K) | $\log(R_{in})$ (cm) | $\log L_*$ (L_\odot) | M_e (M_\odot) |
| M 33 - 1 | 8.17 | 595 | 16.15 | 5.58 | 0.102 | 8.05 | 701 | 16.09 | 5.62 | 0.077 | 5.88 | 900 | 15.96 | 5.66 | 0.031 |
| M 33 - 3 | 2.50 | 400 | 16.61 | 5.69 | 0.261 | 2.67 | 460 | 16.54 | 5.59 | 0.202 | 1.89 | 400 | 16.92 | 5.76 | 0.821 |
| M 33 - 4 | 3.14 | 400 | 16.56 | 5.58 | 0.260 | 3.52 | 400 | 16.68 | 5.58 | 0.507 | 4.53 | 614 | 16.26 | 5.72 | 0.094 |
| M 33 - 7 | 3.69 | 400 | 16.59 | 5.64 | 0.351 | 4.11 | 400 | 16.71 | 5.66 | 0.679 | 3.18 | 400 | 16.91 | 5.74 | 1.321 |
| N 300 - 1 | 6.52 | 501 | 16.41 | 5.72 | 0.271 | 6.89 | 504 | 16.52 | 5.74 | 0.475 | 5.47 | 500 | 16.69 | 5.75 | 0.824 |
| N 2403 - 2 | 3.13 | 401 | 16.63 | 5.72 | 0.358 | 2.99 | 493 | 16.45 | 5.56 | 0.149 | 1.89 | 408 | 16.88 | 5.73 | 0.683 |
| N 2403 - 3 | 18.58 | 404 | 16.71 | 5.86 | 3.070 | 9.41 | 405 | 16.81 | 5.86 | 2.466 | 6.55 | 417 | 16.92 | 5.83 | 2.849 |
| N 2403 - 4 | 5.91 | 400 | 16.74 | 5.93 | 1.121 | 7.09 | 300 | 17.32 | 6.33 | 19.435 | 4.92 | 1182 | 15.75 | 5.91 | 0.010 |
| N 2403 - 5 | 2.78 | 400 | 16.71 | 5.89 | 0.460 | 2.96 | 400 | 16.82 | 5.87 | 0.812 | 1.55 | 400 | 16.99 | 5.91 | 0.928 |
| M 81 - 5 | 14.32 | 514 | 16.32 | 5.58 | 0.393 | 16.83 | 548 | 16.35 | 5.55 | 0.530 | 19.68 | 587 | 16.41 | 5.54 | 0.817 |
| M 81 - 6 | 14.55 | 535 | 16.25 | 5.52 | 0.289 | 16.18 | 559 | 16.30 | 5.50 | 0.405 | 13.09 | 558 | 16.45 | 5.49 | 0.653 |
| M 81 - 11 | 2.81 | 406 | 16.66 | 5.80 | 0.369 | 2.67 | 498 | 16.47 | 5.64 | 0.146 | 1.47 | 432 | 16.85 | 5.78 | 0.463 |
| M 81 - 12 | 3.77 | 399 | 16.67 | 5.79 | 0.518 | 3.99 | 400 | 16.78 | 5.79 | 0.910 | 2.59 | 400 | 16.95 | 5.81 | 1.295 |
| M 81 - 14 | 21.78 | 350 | 16.91 | 5.97 | 9.040 | 21.43 | 400 | 16.81 | 5.84 | 5.613 | 22.28 | 430 | 16.90 | 5.83 | 8.834 |
| N 7793 - 3 | ... | ... | ... | ... | ... | ... | ... | ... | ... | ... | ... | ... | ... | ... | ... |
| N 7793 - 9 | 7.50 | 400 | 16.61 | 5.66 | 0.506 | 8.00 | 400 | 16.77 | 5.76 | 0.629 | 7.00 | 402 | 17.02 | 5.96 | 1.516 |
| N 7793 - 10 | 2.73 | 500 | 16.19 | 5.30 | 0.584 | 2.74 | 500 | 16.27 | 5.25 | 1.030 | 1.12 | 500 | 16.45 | 5.30 | 1.371 |
| N 7793 - 13 | 5.74 | 300 | 17.34 | 6.60 | 0.528 | 5.89 | 400 | 17.16 | 6.53 | 0.923 | 4.29 | 400 | 17.32 | 6.55 | 1.224 |
| IRC+10420 | 5.08 | 401 | 16.60 | 5.66 | 0.782 | 5.25 | 424 | 16.64 | 5.63 | 1.743 | 4.00 | 400 | 16.89 | 5.70 | 4.823 |
| M 33 Var A | 3.37 | 400 | 16.72 | 5.90 | 0.041 | 3.59 | 400 | 16.83 | 5.89 | 0.060 | 2.18 | 400 | 17.00 | 5.92 | 0.056 |
| η Car | 3.67 | 400 | 16.68 | 5.82 | 17.258 | 3.86 | 400 | 16.79 | 5.81 | 7.732 | 2.45 | 400 | 16.95 | 5.83 | 11.767 |

Table 5: Best Fit Models for Silicate Dust and Fixed Temperature

| ID | $T_* = 5000 K$ | | | | | $T_* = 7500 K$ | | | | | $T_* = 20000 K$ | | | | |
|-------------|----------------|--------------|------------------------|-----------------------------|------------------------|----------------|--------------|------------------------|-----------------------------|------------------------|-----------------|--------------|------------------------|-----------------------------|------------------------|
| | τ_V | T_d (K) | $\log(R_{in})$ (cm) | $\log L_*$ (L_\odot) | M_e (M_\odot) | τ_V | T_d (K) | $\log(R_{in})$ (cm) | $\log L_*$ (L_\odot) | M_e (M_\odot) | τ_V | T_d (K) | $\log(R_{in})$ (cm) | $\log L_*$ (L_\odot) | M_e (M_\odot) |
| M 33 – 1 | 14.42 | 816 | 15.58 | 5.56 | 0.013 | 14.26 | 973 | 15.59 | 5.59 | 0.014 | 10.86 | 1204 | 15.75 | 5.67 | 0.022 |
| M 33 – 3 | 4.30 | 592 | 15.83 | 5.75 | 0.012 | 4.66 | 654 | 15.88 | 5.68 | 0.017 | 3.36 | 696 | 16.20 | 5.77 | 0.053 |
| M 33 – 4 | 5.26 | 513 | 15.90 | 5.65 | 0.021 | 5.64 | 601 | 15.89 | 5.58 | 0.021 | 2.58 | 400 | 16.87 | 5.66 | 0.892 |
| M 33 – 7 | 5.91 | 523 | 15.91 | 5.68 | 0.025 | 6.49 | 600 | 15.93 | 5.64 | 0.030 | 5.41 | 604 | 16.31 | 5.79 | 0.142 |
| N 300 – 1 | 10.72 | 724 | 15.76 | 5.77 | 0.022 | 10.99 | 800 | 15.80 | 5.74 | 0.027 | 9.17 | 922 | 16.03 | 5.80 | 0.066 |
| N 2403 – 2 | 5.56 | 583 | 15.89 | 5.80 | 0.021 | 5.66 | 641 | 15.92 | 5.73 | 0.025 | 3.65 | 702 | 16.20 | 5.78 | 0.058 |
| N 2403 – 3 | 21.93 | 469 | 16.18 | 5.90 | 0.316 | 19.50 | 501 | 16.24 | 5.91 | 0.370 | 16.98 | 651 | 16.31 | 5.85 | 0.445 |
| N 2403 – 4 | 9.81 | 505 | 16.09 | 5.93 | 0.093 | 9.72 | 1114 | 15.58 | 5.82 | 0.009 | 7.95 | 1499 | 15.64 | 5.85 | 0.010 |
| N 2403 – 5 | 5.30 | 502 | 16.10 | 6.03 | 0.053 | 5.35 | 600 | 16.06 | 5.93 | 0.044 | 3.41 | 628 | 16.39 | 6.00 | 0.129 |
| M 81 – 5 | 28.38 | 616 | 15.86 | 5.63 | 0.094 | 28.71 | 705 | 15.85 | 5.59 | 0.090 | 24.38 | 913 | 15.94 | 5.59 | 0.116 |
| M 81 – 6 | 37.84 | 655 | 15.79 | 5.55 | 0.090 | 35.40 | 722 | 15.81 | 5.53 | 0.093 | 29.17 | 957 | 15.87 | 5.52 | 0.101 |
| M 81 – 11 | 5.26 | 586 | 15.93 | 5.90 | 0.024 | 5.38 | 650 | 15.96 | 5.83 | 0.028 | 3.36 | 702 | 16.25 | 5.88 | 0.067 |
| M 81 – 12 | 7.16 | 410 | 16.26 | 6.00 | 0.149 | 7.33 | 500 | 16.21 | 5.93 | 0.121 | 5.62 | 517 | 16.55 | 6.05 | 0.444 |
| M 81 – 14 | 26.85 | 400 | 16.34 | 5.95 | 0.808 | 25.47 | 496 | 16.23 | 5.85 | 0.462 | 21.68 | 601 | 16.36 | 5.85 | 0.715 |
| N 7793 – 3 | ... | ... | ... | ... | ... | ... | ... | ... | ... | ... | ... | ... | ... | ... | ... |
| N 7793 – 9 | 8.42 | 585 | 15.85 | 5.68 | 0.027 | 8.67 | 617 | 15.93 | 5.65 | 0.039 | 6.80 | 701 | 16.16 | 5.70 | 0.089 |
| N 7793 – 10 | 6.24 | 472 | 16.17 | 6.05 | 0.086 | 6.56 | 512 | 16.23 | 6.03 | 0.119 | 4.56 | 600 | 16.44 | 6.05 | 0.217 |
| N 7793 – 13 | 6.53 | 484 | 16.10 | 5.94 | 0.065 | 6.88 | 500 | 16.21 | 5.93 | 0.114 | 4.81 | 589 | 16.41 | 5.95 | 0.200 |
| IRC+10420 | 10.99 | 600 | 15.73 | 5.44 | 0.020 | 11.51 | 700 | 15.77 | 5.48 | 0.025 | 10.00 | 1000 | 15.86 | 5.57 | 0.033 |
| M 33 Var A | 5.04 | 793 | 15.44 | 5.36 | 0.002 | 5.03 | 867 | 15.48 | 5.28 | 0.003 | 2.67 | 962 | 15.75 | 5.33 | 0.005 |
| η Car | 9.94 | 250 | 17.08 | 6.76 | 9.026 | 10.42 | 300 | 17.05 | 6.78 | 8.245 | 8.49 | 400 | 17.12 | 6.80 | 9.272 |